REPORT DOCUMENTATION PAGE

The public reporting burden for this collection of information is estimated to average 1 hour per response, including the time for reviewing instructions, searching existing data sources, gathering and maintaining the data needed, and completing and reviewing the collection of information. Send comments regarding this burden estimate or any other aspect of this collection of information, including suggestions for reducing the burden, to Department of Defense, Washington Headquarters Services, Directorate for Information Operations and Reports (0704-0188), 1215 Jefferson Davis Highway, Suite 1204, Arlington, VA 22202-4302. Respondents should be aware that notwithstanding any other provision of law, no person shall be subject to any penalty for failing to comply with a collection of information if it does not display a currently valid OMB control number.
PLEASE DO NOT RETURN YOUR FORM TO THE ABOVE ADDRESS.

1. REPORT DATE (DD-MM-YYYY)	2. REPORT TYPE	3. DATES COVERED (From - To)
10/21/2016	Final Report	08/01/2013-07/31/2016

4. TITLE AND SUBTITLE
Seeded Reaction Waves in Composites: Fast Structure-Transforming Materials that Respond to Energetic Stimuli

5a. CONTRACT NUMBER

5b. GRANT NUMBER
N00014-13-1-0170

5c. PROGRAM ELEMENT NUMBER

6. AUTHOR(S)
Prof. Jeff Moore, Prof. Paul Braun, Prof. Nancy Sottos, Prof. Scott White, Dr. Pengcheng Sun, Dr. Jinyun Liu, Dr. Nina Sekerak, Dr. Kristin Hutchins, Dr. Jun Li, Ian Robertson

5d. PROJECT NUMBER

5e. TASK NUMBER

5f. WORK UNIT NUMBER

7. PERFORMING ORGANIZATION NAME(S) AND ADDRESS(ES)
The Board of Trustees of the University of Illinois at Urbana-Champaign
Grants and Contracts Office
1901 South First Street, Suite A
Champaign, IL 61820-7406

8. PERFORMING ORGANIZATION REPORT NUMBER

9. SPONSORING/MONITORING AGENCY NAME(S) AND ADDRESS(ES)
Office of Naval Research
875 North Randolph Street
Arlington, VA 22203-1995

10. SPONSOR/MONITOR'S ACRONYM(S)
ONR

11. SPONSOR/MONITOR'S REPORT NUMBER(S)
703-696-3073

12. DISTRIBUTION/AVAILABILITY STATEMENT
Approved for Public Release: distribution is Unlimited

13. SUPPLEMENTARY NOTES

14. ABSTRACT

Damage in polymer and composite materials is often rapid and catastrophic. Preventing damage requires a new class of material that can autonomically respond to imminent damage by rapidly changing its physical properties. Herein we report several mechanisms by which autonomic material self-protection may be realized. The incorporation of encapsulated super-cooled fluids into a polymer matrix allows for rapid changes in mechanical properties. Frontal polymerization within a microvascular network rapidly forms an endoskeletal structure within a flexible rubber, stiffening it up to 18x. Polymer seed particles have also been developed towards enabling a seeded frontal polymerization. Mechanochemical activity at interfac

15. SUBJECT TERMS
Seeded reaction, rapid transformation, mechanochemistry, supercooled microcapsules, frontal polymerization

16. SECURITY CLASSIFICATION OF:			17. LIMITATION OF ABSTRACT	18. NUMBER OF PAGES	19a. NAME OF RESPONSIBLE PERSON
a. REPORT	b. ABSTRACT	c. THIS PAGE			Jeffrey S. Moore
U	U	U	SAR	39	19b. TELEPHONE NUMBER (Include area code) 217.244.5289

INSTRUCTIONS FOR COMPLETING SF 298

1. REPORT DATE. Full publication date, including day, month, if available. Must cite at least the year and be Year 2000 compliant, e.g. 30-06-1998; xx-06-1998; xx-xx-1998.

2. REPORT TYPE. State the type of report, such as final, technical, interim, memorandum, master's thesis, progress, quarterly, research, special, group study, etc.

3. DATE COVERED. Indicate the time during which the work was performed and the report was written, e.g., Jun 1997 - Jun 1998; 1-10 Jun 1996; May - Nov 1998; Nov 1998.

4. TITLE. Enter title and subtitle with volume number and part number, if applicable. On classified documents, enter the title classification in parentheses.

5a. CONTRACT NUMBER. Enter all contract numbers as they appear in the report, e.g. F33315-86-C-5169.

5b. GRANT NUMBER. Enter all grant numbers as they appear in the report. e.g. AFOSR-82-1234.

5c. PROGRAM ELEMENT NUMBER. Enter all program element numbers as they appear in the report, e.g. 61101A.

5e. TASK NUMBER. Enter all task numbers as they appear in the report, e.g. 05; RF0330201; T4112.

5f. WORK UNIT NUMBER. Enter all work unit numbers as they appear in the report, e.g. 001; AFAPL30480105.

6. AUTHOR(S). Enter name(s) of person(s) responsible for writing the report, performing the research, or credited with the content of the report. The form of entry is the last name, first name, middle initial, and additional qualifiers separated by commas, e.g. Smith, Richard, J, Jr.

7. PERFORMING ORGANIZATION NAME(S) AND ADDRESS(ES). Self-explanatory.

8. PERFORMING ORGANIZATION REPORT NUMBER. Enter all unique alphanumeric report numbers assigned by the performing organization, e.g. BRL-1234; AFWL-TR-85-4017-Vol-21-PT-2.

9. SPONSORING/MONITORING AGENCY NAME(S) AND ADDRESS(ES). Enter the name and address of the organization(s) financially responsible for and monitoring the work.

10. SPONSOR/MONITOR'S ACRONYM(S). Enter, if available, e.g. BRL, ARDEC, NADC.

11. SPONSOR/MONITOR'S REPORT NUMBER(S). Enter report number as assigned by the sponsoring/ monitoring agency, if available, e.g. BRL-TR-829; -215.

12. DISTRIBUTION/AVAILABILITY STATEMENT. Use agency-mandated availability statements to indicate the public availability or distribution limitations of the report. If additional limitations/ restrictions or special markings are indicated, follow agency authorization procedures, e.g. RD/FRD, PROPIN, ITAR, etc. Include copyright information.

13. SUPPLEMENTARY NOTES. Enter information not included elsewhere such as: prepared in cooperation with; translation of; report supersedes; old edition number, etc.

14. ABSTRACT. A brief (approximately 200 words) factual summary of the most significant information.

15. SUBJECT TERMS. Key words or phrases identifying major concepts in the report.

16. SECURITY CLASSIFICATION. Enter security classification in accordance with security classification regulations, e.g. U, C, S, etc. If this form contains classified information, stamp classification level on the top and bottom of this page.

17. LIMITATION OF ABSTRACT. This block must be completed to assign a distribution limitation to the abstract. Enter UU (Unclassified Unlimited) or SAR (Same as Report). An entry in this block is necessary if the abstract is to be limited.

Final Report: N00014-13-1-0170

Seeded Reaction Waves in Composites: Fast-Structure-Transforming Materials that Respond to Energetic Stimuli

Lead PI: Jeff Moore

Co-PIs: Paul Braun, Nancy Sottos and Scott White

University of Illinois at Urbana-Champaign

August 1, 2013-July 31, 2016

Supercooled Liquid-Filled Capsules

Postdoc (PI): Dr. Jinyun Liu (Braun), Dr. Pengcheng Sun (Braun)

Purpose:

To design, synthesize, and encapsulate liquids which can exist as a supercooled fluid below the normal melting temperature, and then crystallize into a solid when triggered. We anticipate upon an external triggering event, that the liquid will rapidly crystalize. If capsules containing such a supercooled liquid are embedded in a matrix, the mechanical properties of the matrix will be a function of the physical state of the material within the capsules, thus enabling formation of a material with rapidly switchable mechanics.

Work completed:

As illustrated in Scheme 1, materials with supercooling potential are encapsulated into capsules. Once the material in the capsule is in the molten state, it tends to remain in the molten state, even below the normal freezing point. Then, upon application of an appropriate stimulus, the liquid will crystallize. This process is reversible. On the basis of such hypothesis, we achieved high quality encapsulation of a series of organics such as long chain alkanes C_8H_{18}, $C_{16}H_{34}$, $C_{20}H_{42}$, $C_{22}H_{46}$ and $C_{26}H_{54}$ (both single and their mixtures). Their thermal properties have been investigated, and interesting results have been obtained.
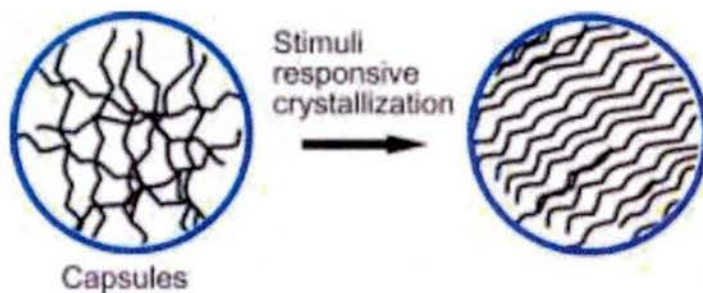
Scheme 1. Illustration of the energy-introduced crystallization. The material in the left capsule is a liquid, and the material in the right capsule is a crystalline solid.

To determine the conditions for high quality encapsulation of alkanes, we start with a short chain alkane (C_8H_{18}), which is a liquid at room temperature. We find the reaction time is a very important factor to affect the shell thickness and surface morphology of the capsule, and from the SEM(Figure.1) we can observe that around 2 hours is the best reaction time to produce high quality alkanes capsules, shorter time periods (e.g. 1 h) or longer periods (above 4 h) will produce capsules that are either inseparable or shows rough surface morphology with PUF polymer particles adhered.
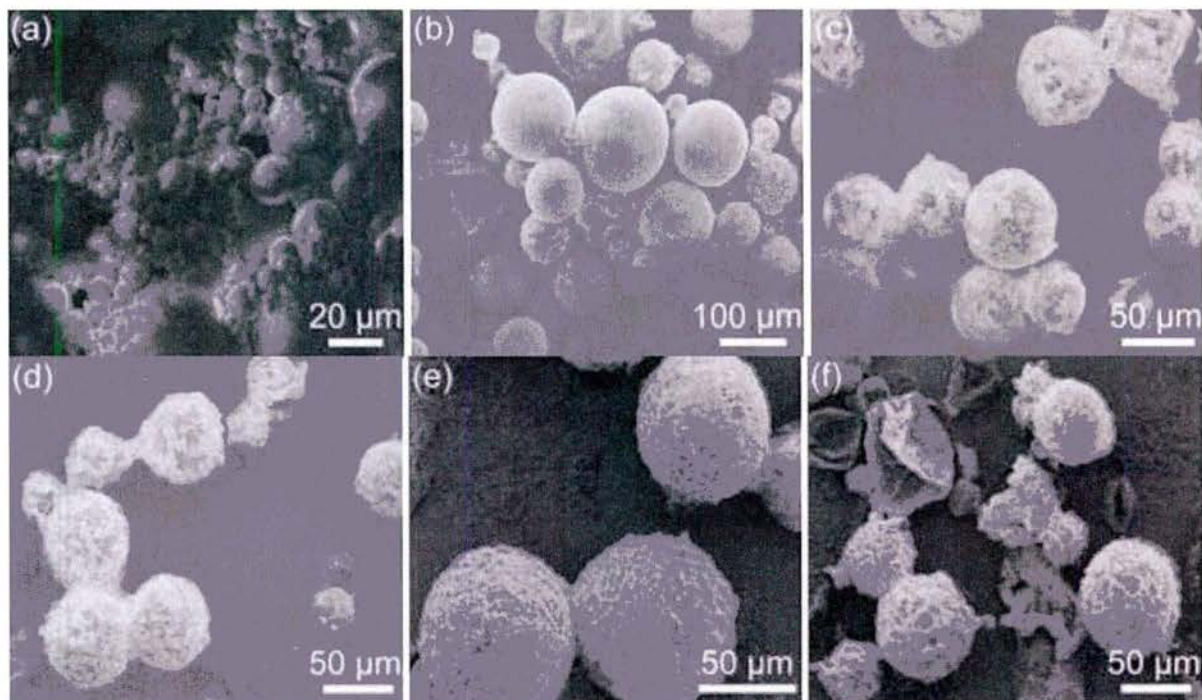
Figure 1. SEM images of microcapsules (C_8H_{18} as core materials) prepared under different reaction time: (a) 1 h, (b)2 h, (c) 3 h, (d) 4 h, (e) 5 h, and (f) 6 h.

We also find out the relationship between reaction time and microcapsules size distributions. Increasing reaction time produces more uniform size of capsules due to an Ostwald ripening mechanism. The ratio of core to shell material (i.e., C8: urea plus formaldehyde) determines the product yields (the ratio of about 0.9 comes out satisfying yield). In this condition, we barely see oil in the upper layer, and only a little PUF at the bottom layer after a week. Otherwise, if using a relatively high ratio (e.g., 1.1), there is no oil floats in upper layer, and more than 3/4 of the system is PUF, resulting in a very low yield.

The surfactant (EMA was employed here), is crucial for the emulsification and to ensure the organic core material droplets remain stable in aqueous solution without agglomeration. Figure 2 shows the size distribution of microcapsules prepared using different amount of surfactants. We can see the size distribution becomes much more uniform when the surfactant increases to 30 ml. Too much of surfactant leads to a lot of bubbles, and makes the solution difficult to separate.
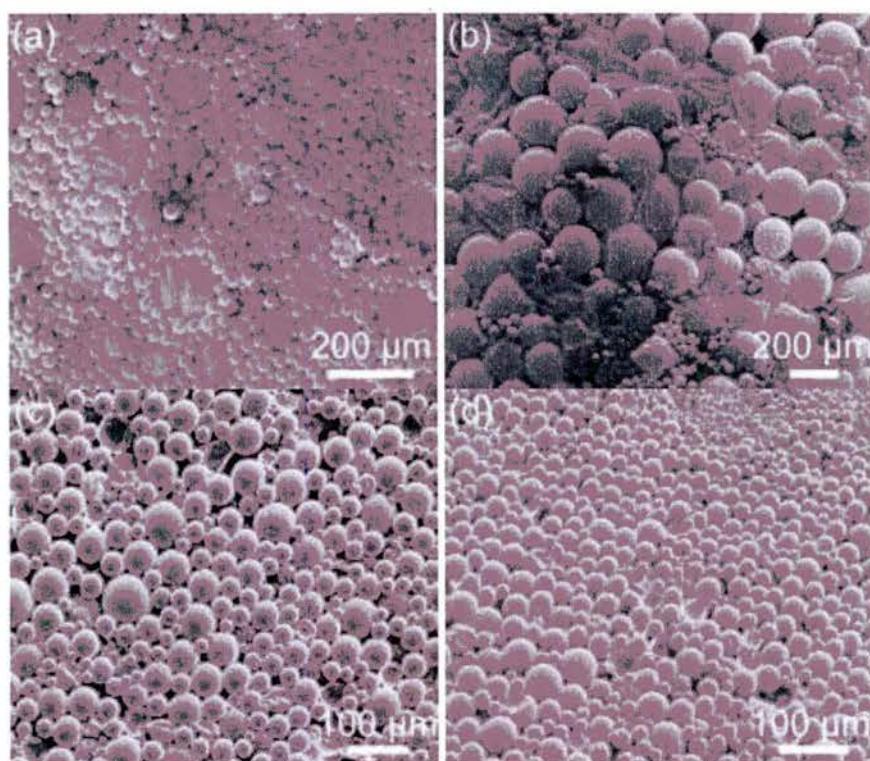
Figure 2. SEM images of microcapsules (C_8H_{18} as core materials) prepared using different amounts of EMA: (a) 24ml, (b) 25 ml, (c) 30 ml, and (d) 38 ml.

Since we obtain the preparation conditions for high quality alkane encapsulation, we extend and improve our investigations on encapsulation of $C_{16}H_{34}$ and $C_{20}H_{42}$ which are phase transition materials with melting temperature around 18 ℃ and 36-38 ℃ respectively. From the SEM analysis performed for $C_{16}H_{34}$ capsule at room temperature (Figure 3), we can see that the capsule is spherical without obvious collapse, indicating that the core material is full inside the capsules. In Figure 4, we can see that the three peaks appear in cooling process of DSC curves, with the first cooling peak at about 1.2 ℃ (melting temperature about 20 ℃), showing significant super-cooling performance.
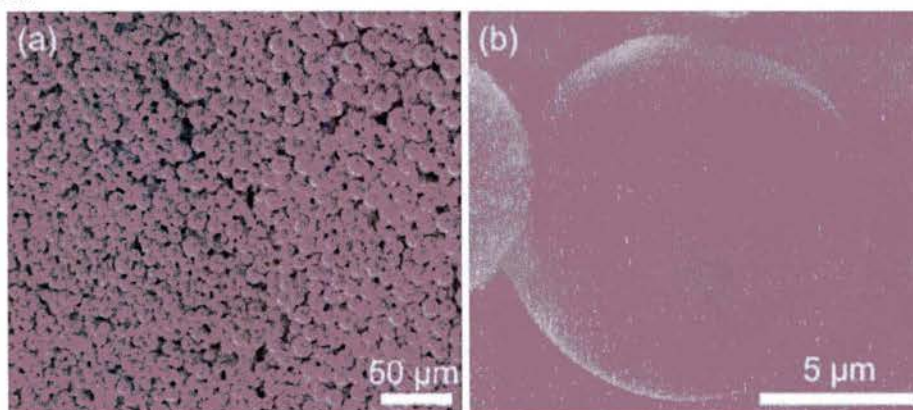
**Figure 3.** SEM images of the prepared $C_{16}H_{34}$ microcapsules.
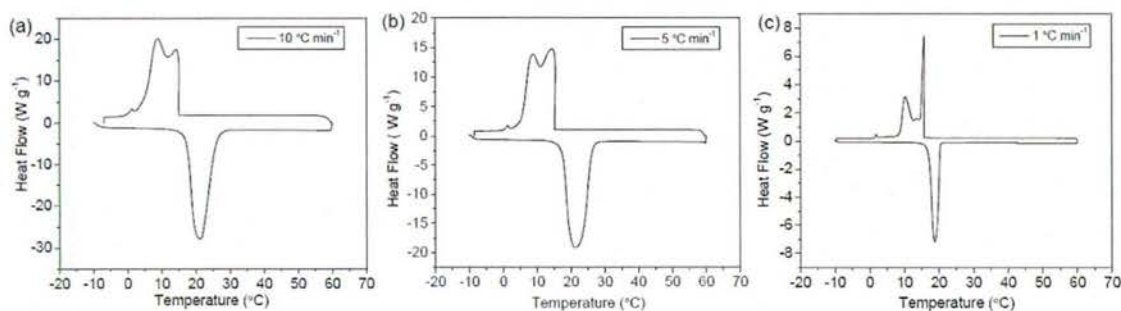
Figure 4. DSC curves of $C_{16}H_{34}$ capsules (~20 μm) in different heating-cooling rates: (a) 10 ºC min-1; (b)5 ºC min-1; (c) 1 ºC min-1.

The heating-cooling process of $C_{16}H_{34}$ capsules (~20 μm) observed under polarizers in transmittance mode of optical microscope was also performed, as shown in Figure 5. The capsules become dark at around 21 ºC, and remain the same throughout the heating cycle. In cooling process, light spots appear at 13 ºC and continue to increase, indicating the crystallization occurs. The quantity of light spots keeps the same after it reaches 7 ºC, and it was not until –9 ºC that the capsule begins another transformation and the light spots increases again, showing crystallization at different stages.
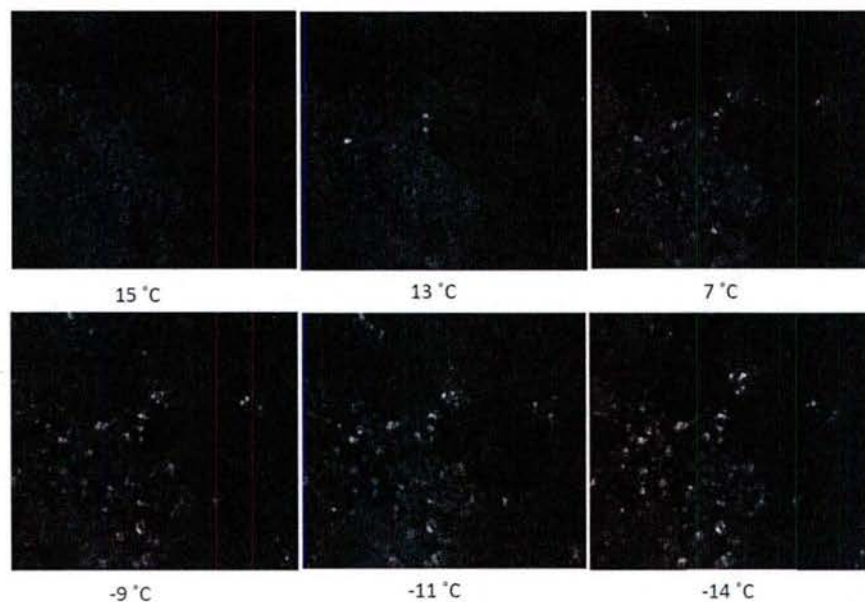
Heating:
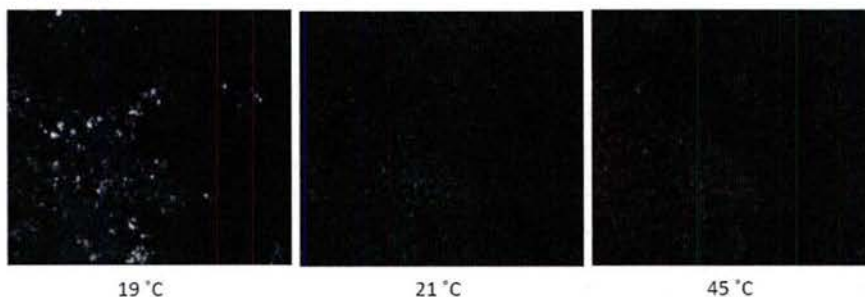
Cooling:

Figure 5. Optical images of $C_{16}H_{34}$ capsules by using polarizers during heating-cooling process.

we encapsulated long chain alkanes e.g. icosane ($C_{20}H_{42}$) inside polymer capsules prepared from polyureaformaldehyde (PUF). The morphology (SEM images) of the capsules and the thermal behavior (DSC measurements) are shown in Figure 6.
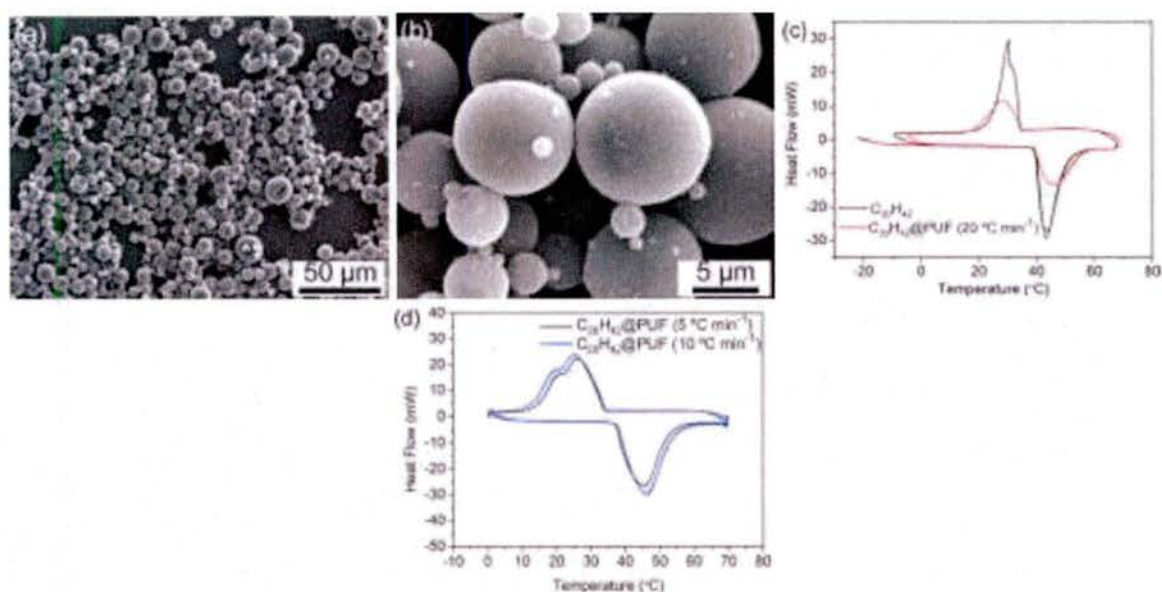

Figure 6. SEM images (a, b), and the DSC curves of the C20H42 and the PUF capsules encapsulated with $C_{20}H_{42}$ at a heating/cooling rate of 20 °C min^{-1} (c), and 10 and 5 °C min^{-1} (d).

By DSC, the long chain alkanes showed a supercooling of about 10 to 15 °C in both pure form and in the encapsulated state at a heating and cooling rate of 20 °C min-1 (Figure 1c). We also used different heating/cooling rates (5 and 10 °C min-1) to determine the rate dependence of the thermal behavior of the capsules, and the degree of supercooling remained about the same. To increase the capsule stability, the capsules were coated with a SiO_2 layer and the thermal properties were measured (Figure 7). The general melting and recrystallization temperatures were same as for the uncoated capsules, however, multiple peaks were observed in the recrystallization process, which requires further investigation.
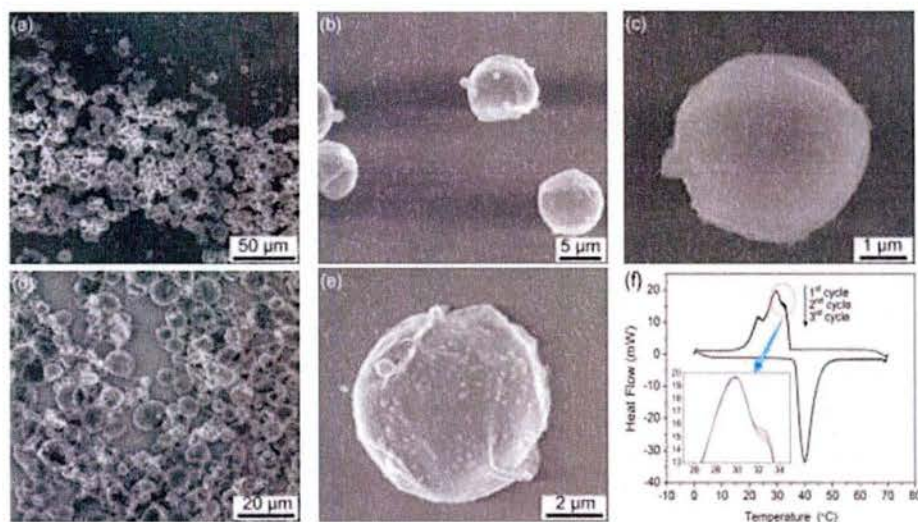
Figure 7. Low- and high-magnification SEM images of the SiO$_2$-coated capsules (a-c). Low (d) and high (e) magnification images of the capsules after thermal removal of core materials (SiO$_2$ coatings remained only). DSC (f) of SiO$_2$-coated capsules encapsulated with alkane at heating and cooling rate of 20 °C min^{-1}.

We also used different emulsification speeds for encapsulation of the C$_{20}$H$_{42}$ capsule. In Figure 8, we can see the capsule size is very large (> 400 μm) at an emulsification speed of 1200 rpm; while the size is about 50 μm and 20um at 2000 rpm and 3000 rpm respectively. The thermal properties of the microcapsules have been analyzed by DSC. Figure 9-11 show the DSC curve for the C$_{20}$H$_{42}$ capsules with three different sizes.
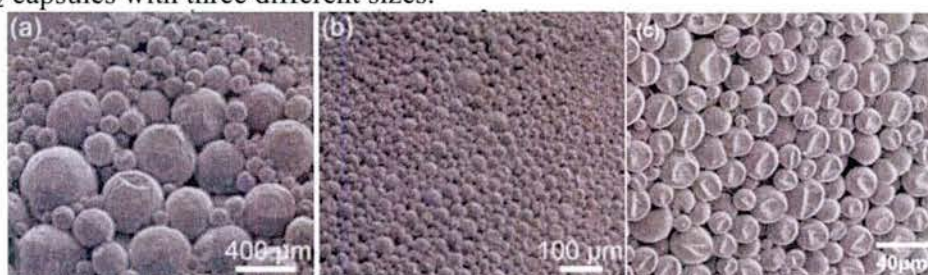

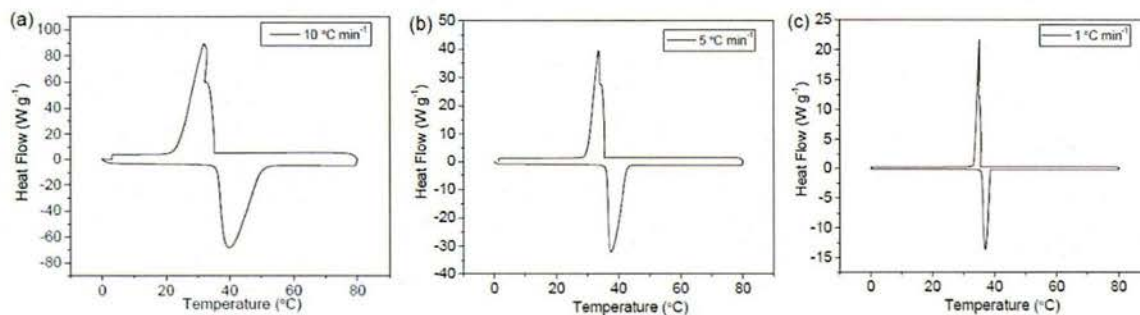**Figure 8.** SEM images of C$_{20}$H$_{42}$ microcapsules prepared at (a) 1200 rpm and (b) 2000 rpm. (c)3000 rpm.

Figure 9. DSC curves of $C_{20}H_{42}$ capsules of about 200 μm in different heating-cooling rates: (a) 10 °Cmin^{-1}; (b) 5 °C min^{-1}; (c) 1 °C min^{-1}.

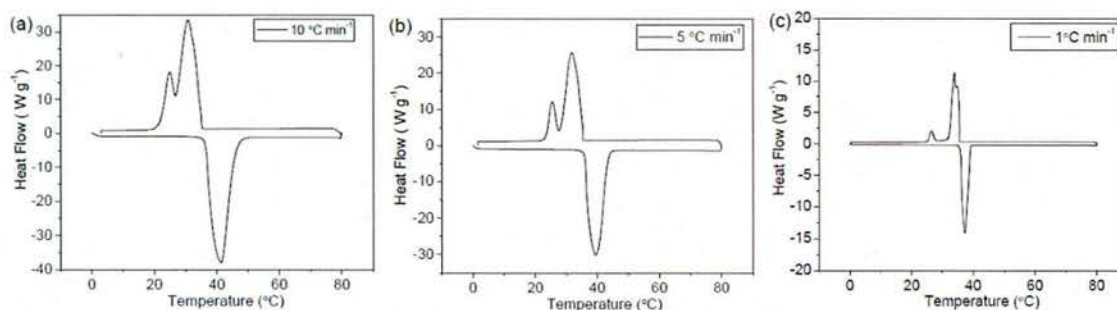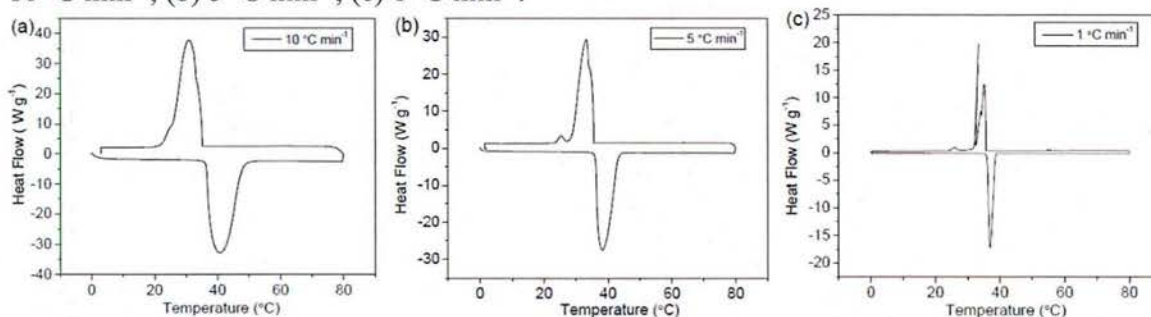**Figure 10.** DSC curves of $C_{20}H_{42}$ capsules of about 50 μm in different heating-cooling rates: (a) 10 °C min^{-1}; (b) 5 °C min^{-1}; (c) 1 °C min^{-1}.

Figure 11. DSC curves of $C_{20}H_{42}$ capsules of about 20 μm in different heating-cooling rates: (a) 10 °C min^{-1}; (b) 5 °C min^{-1}; (c) 1 °C min^{-1}.

We recorded the heating-cooling process of capsules with the size of about 20 μm with polarizers in transmittance mode of optical microscope. In Figure 12, capsules change from bright to completely dark at ~39 °C. Interestingly, during cooling process, when the temperature goes down to 37.5-35 °C, capsules begin to show up bright spots, and then images don't change much when the cooling continues. However, starting from 27.5 °C, the bright spots dimmed and decreased, which means another obvious change in the structure of the capsule system. The temperatures at which the capsules undergo transformation are in accordance with the results in DSC curves.
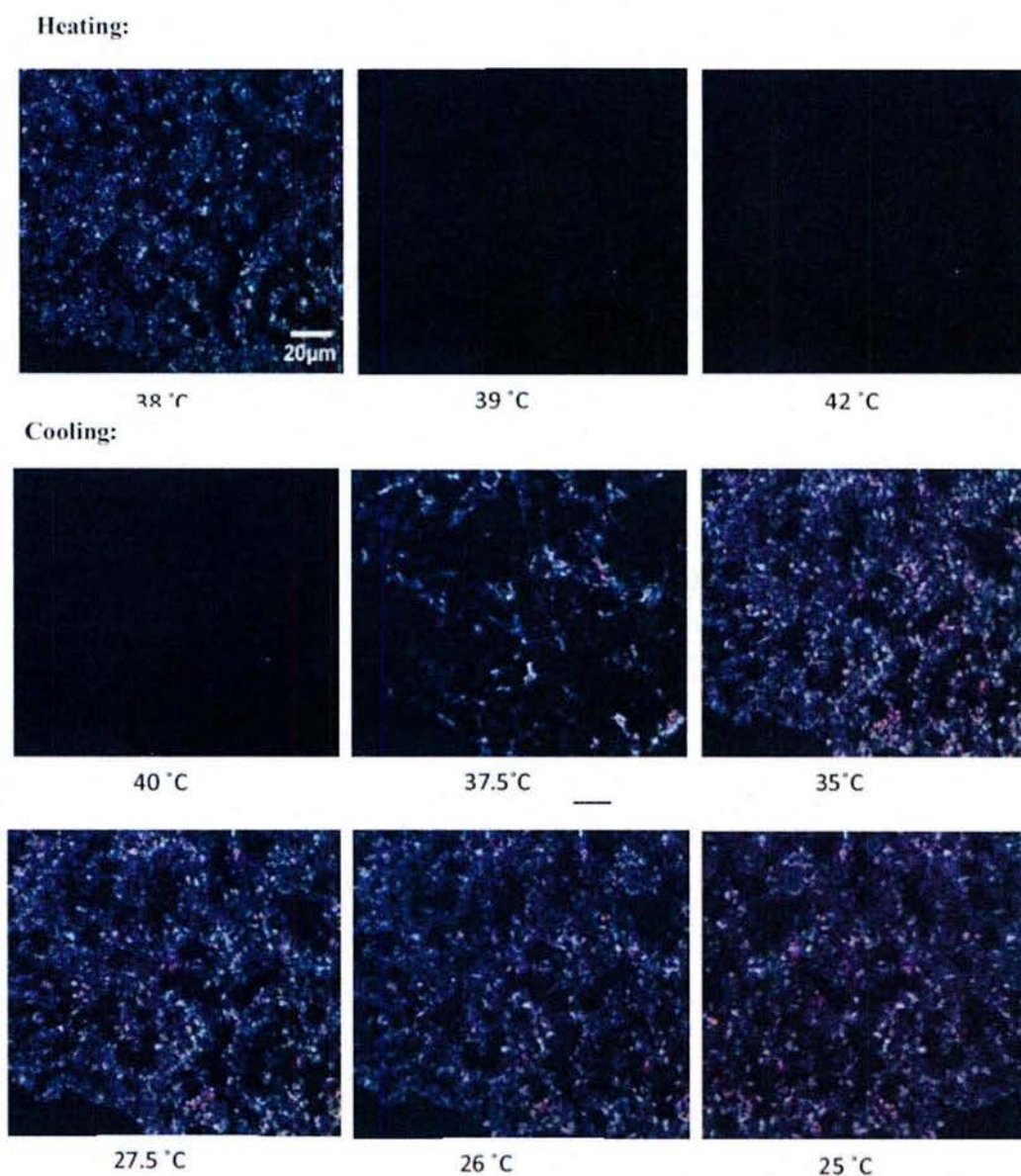
Heating:

38 °C   39 °C   42 °C

Cooling:

40 °C   37.5°C   35°C

27.5 °C   26 °C   25 °C

Figure 12. Optical images (with polarizers) of $C_{20}H_{42}$ capsules during heating-cooling process.

On the basis of these $C_{20}H_{42}$ microcapsules, we conduct the thermal analysis through DSC and TGA, as shown in Figure 13. In Figure 13a, we can see that as the heating/cooling rate increases, the exothermic and endothermic peaks turn to be wide. However, if the rate is too slow, the super-cooling property will be less obvious. Considering that, the $C_{20}H_{42}$ microcapsules were analyzed at a rate of 5 °C min^{-1}. Interestingly, different from pure chemical, there are two divided exothermic peaks (25.3 °C and 31.9 °C), accompanying with an endothermic peaks at 39.5 °C, close to the melting point, perhaps indicating that some capsules super cool more than others. The TGA result (Figure 13c) confirms a good quality of the prepared capsules.
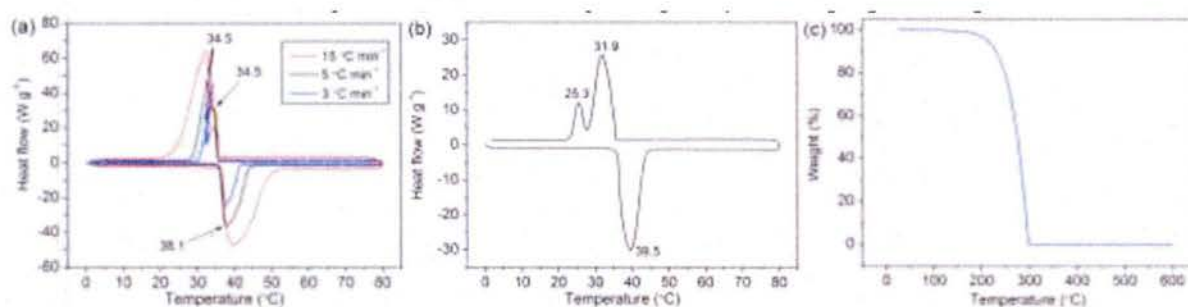
Figure 13. (a) DSC curves of pure $C_{20}H_{42}$ at different heating/cooling rates. (b) DSC curve of $C_{20}H_{42}$ capsules at a heating/cooling rate of 5 °C min-1. (c) TGA curve of $C_{20}H_{42}$ capsules.

We further investigate the phase change of the $C_{20}H_{42}$ capsules using optical microscope under transmittance mode and with polarizers, As shown in Figure 14. In Figure 14a, we can see the capsules turn to transparent from about 43 °C depending on heating up. During cooling process, they return to black start from about 35 °C, and end at about 28 °C. Correspondingly, we investigate the polarization behaviors (Figure 14b), capsules seem to slightly dark until 40-43 °C (whole screen becomes dark). Interestingly, during cooling process, when the temperature goes down to 33-35 °C, capsules show bright spots with shine colors. Below 30 °C, brightness turns to weak gradually.
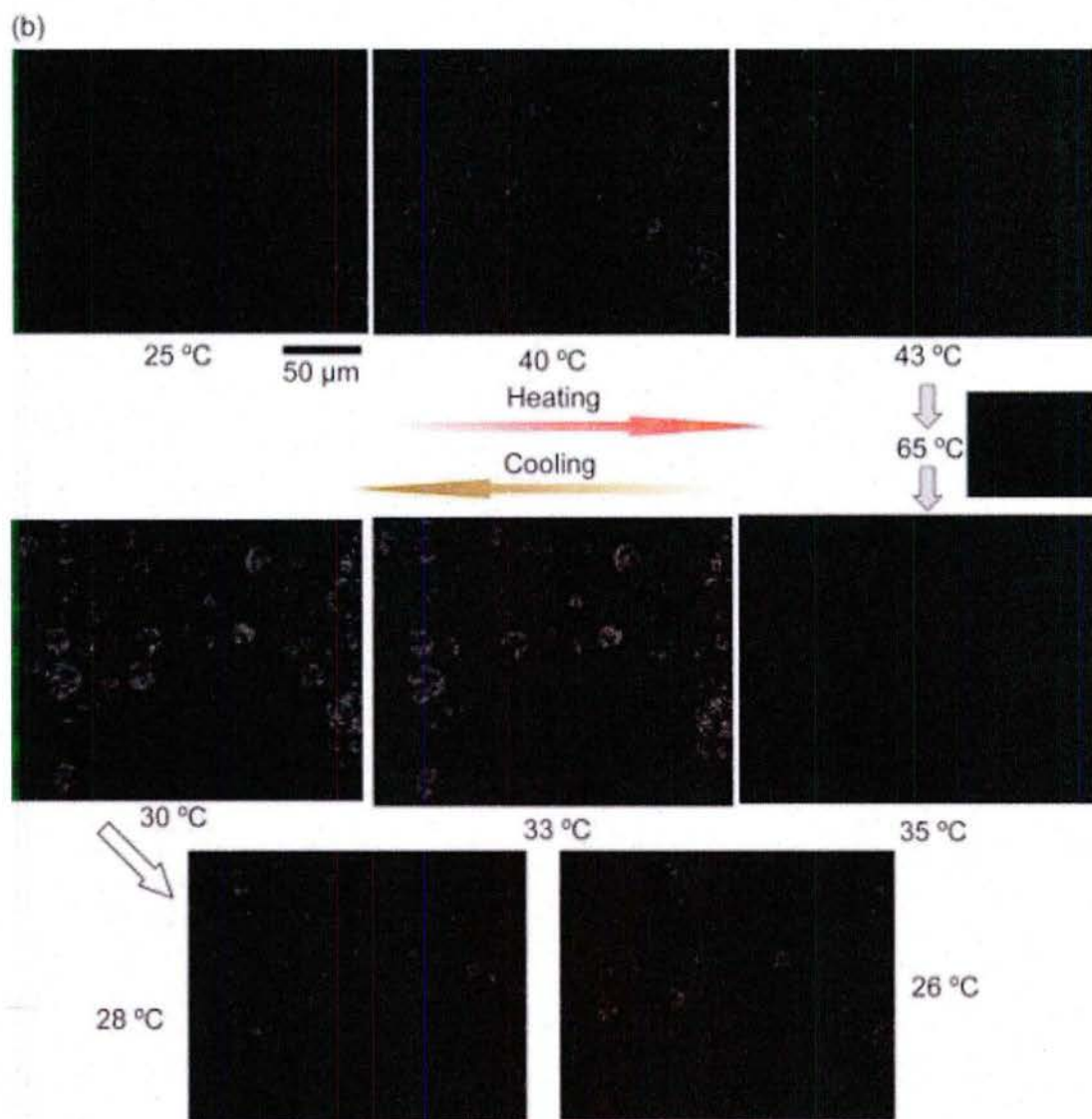
(b)
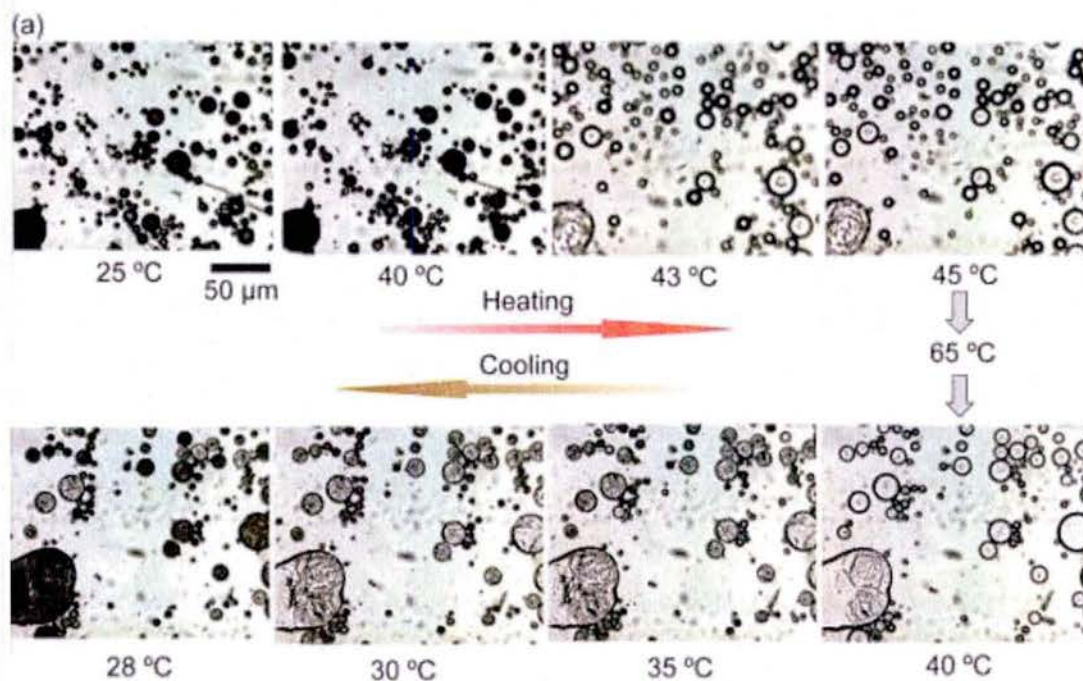
Figure 14. A series of optical images of the $C_{20}H_{42}$ capsules during heating/cooling process: (a) transmittance mode images, (b) polarization images.

We also applied polarization microscopy to investigate the temperature-dependent changes of morphology based on $C_{20}H_{42}$ capsules (Figure 15). Changes in shape and optical rotation (as determined by polarized optical microscopy) with respect to temperature can be used to evaluate phase transitions of encapsulated materials inside the capsules. Melting is observed at 43 °C, and freezing at 38 °C for the eicosane filled capsules (Fig. 15 c,d). In the images the temperature noted is when the optical rotation is last observed on heating, and first observed on cooling.
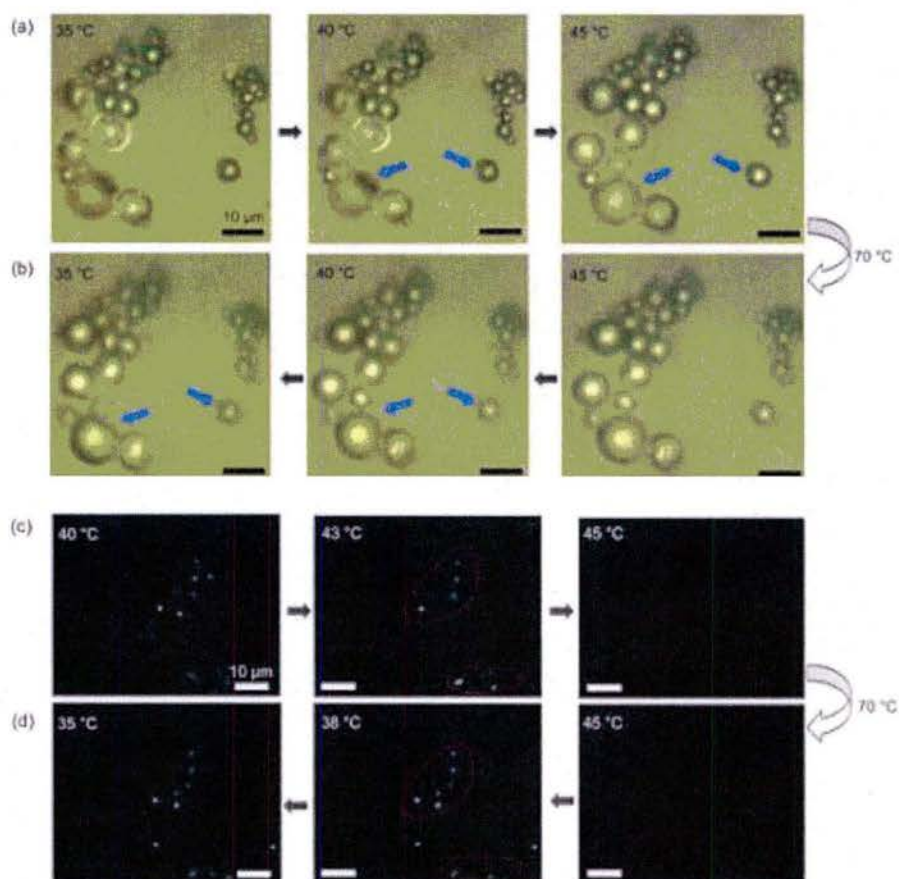
Figure 15. Optical images of eicosane capsules during (a) heating and (b) cooling. (c) and (d) are polarized optical microscopy images also during heating (c) and cooling (d). The ramp rate for both heating and cooling is 5 °C min-1; the temperature range is over 23 to 70 °C.

The capsules encapsulated with long chain alkanes, such as $C_{22}H_{46}$ and $C_{26}H_{54}$ were also synthesized (Figure16). The DSC results are shown in Figure 17. In particular, the capsules with mixture of $C_{22}H_{46}$ and $C_{26}H_{54}$ exhibit some interesting peaks (perhaps because of the interaction between different component within the capsules), which we will keep doing investigations.
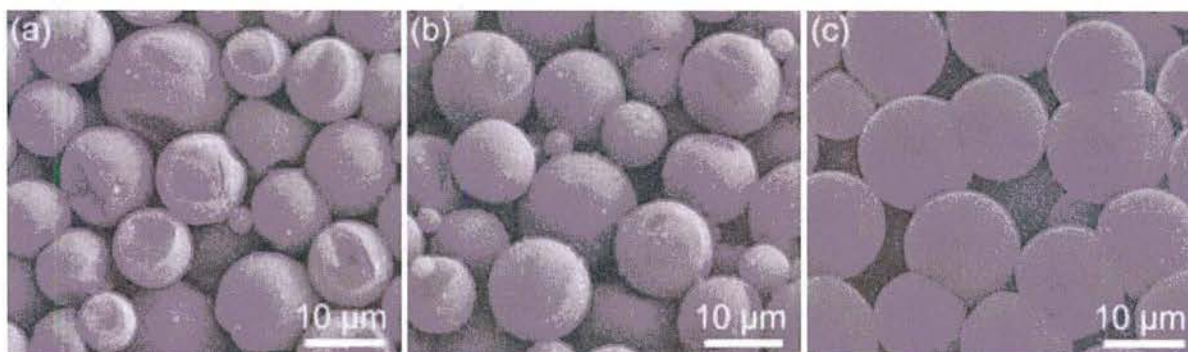

Figure 16. SEM images of microcapsules with different core materials: (a) $C_{22}H_{46}$, (b) $C_{26}H_{54}$, (c) mixture of $C_{22}H_{46}$ and $C_{26}H_{54}$ (1: 1 weight ratio).

Figure 17. DSC curves of capsules with different core materials: (a) $C_{22}H_{46}$, (b) $C_{26}H_{54}$, (c) mixture of $C_{22}H_{46}$ and $C_{26}H_{54}$ (1: 1 weight ratio).
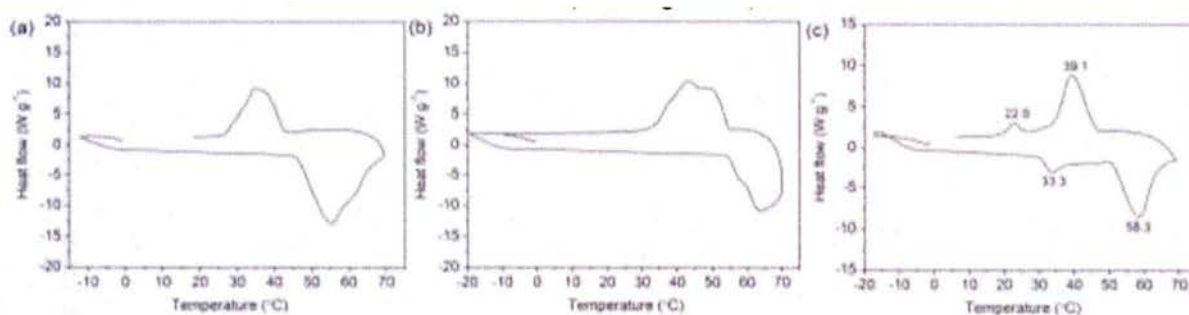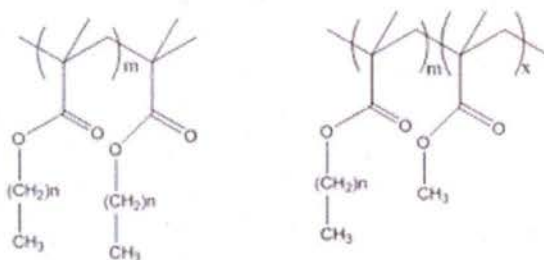
New polymeric architectures expected to provide significant supercooling based on poly (alkyl methacrylates) and poly (lactic acid) were designed and synthesized. The structures of a few example polymers are shown in Scheme 2.


Scheme 2. Structures of the designed poly (alkyl methacrylates)

Synthesis of the monomers for these polymers is based on the reaction of commercially available methacryloyl chloride with long chain alcohols. Polymerization was carried out via radical or living polymerizations to obtain both random and block copolymers. A few polymers have been synthesized and properties were investigated. The melting and re-crystallization behaviors were investigated by using DSC measurements. The data are summarized in Table 1. Supercooling was observed for all systems.

Table 1. The DSC measuring results of different methacrylates.

Polymer	Monomers	Molecular weight	T_m °C		T_c °C	
			Peak	Onset	Peak	Onset
1	Dodecyl methacrylate	Mn=7686, PDI=1.76	-53.4	-41.1	-45.6	-39.3
2	Tetradecyl methacrylate	Mn=33211, PDI=1.74	-6.4	-18	-14.5	-8.8
3	Hexadecyl methacrylate	Mn=37980, PDI=1.78	18.5	9.62	8.8	11.2
4	Octadecyl methacrylate	Mn=16072, PDI=1.59	35.1	29.5	24.9	27.7

Polymethacrylates with polyethylene glycol side chains with broader supercooling ranges were also synthesized. The synthetic scheme for this new polymer is shown in Scheme 3.
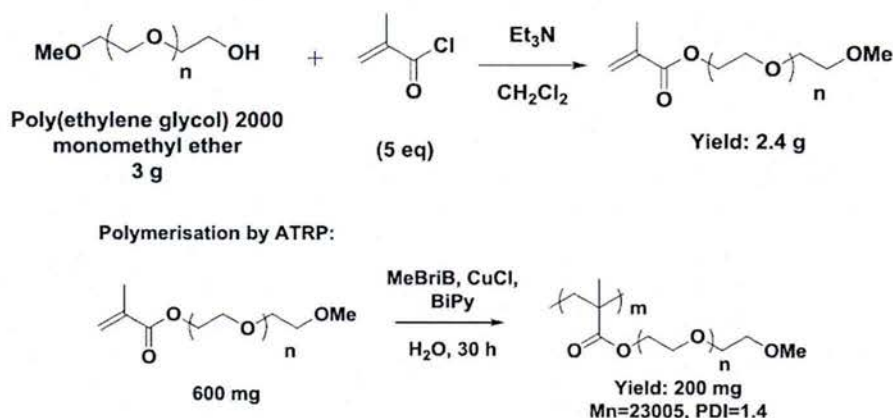
Scheme 3. Synthesis of polymethacrylates with polyethylene glycol side chains.

The new polymer was purified using repeated precipitation from different solvents to remove impurities. From DSC (Figure 18), it is observed that the polymer shows a supercooling of ~19.5 °C. Both block and random copolymers with even larger possible supercoolings are currently being synthesized. The current system, as well as these new polymers will be encapsulated into polymer capsules or inside a stable inert soft matrix, and the thermal properties will be investigated.
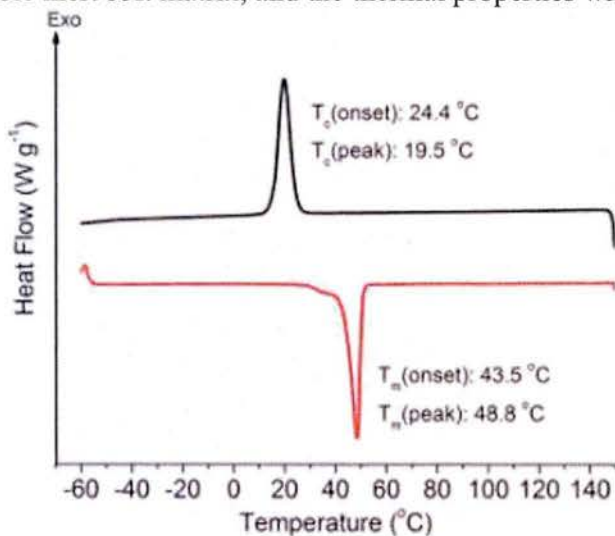

Figure 18. DSC of polyethylene glycol incorporated polymethacryalate. Ramp rate rate: 10 °C min-1.

Many inorganic salt solutions tend to supercool under different conditions. For example, aqueous sodium acetate solutions are well known to supercool, and are sensitive to external triggers such as high impact stress. Encapsulation of supersaturated sodium acetate solution was also attempted using a different double emulsion process. A device surrounds the inner fluid, the sodium acetate solution, with the middle fluid, a polymer shell material dissolved in an organic solvent,

surrounded in turn by a 10 wt.% PVA solution. Two different polymer shell options were explored: poly(lactic acid) and polystyrene. Optical microscopy images are shown for cases in which poly(lactic acid) (Figure 19a) and polystyrene (Figure 19b) were dissolved in chloroform for the encapsulation process. As can be seen from the images, polystyrene does a much better job of forming stable emulsions than poly(lactic acid) due to its higher hydrophobicity, so it was determined to be the superior shell material.
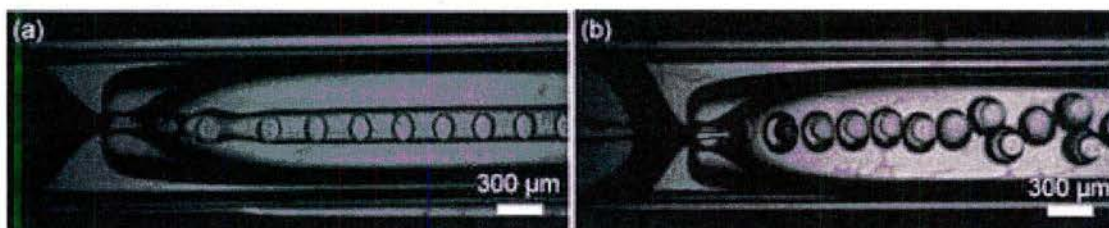

Figure 19. Optical microscopy images of the supersaturated sodium acetate solution encapsulation process using shell material: (a) poly(lactic acid) and (b) polystyrene.

The main problem associated with the encapsulation process is the spontaneous nucleation of sodium acetate trihydrate crystals. When these crystals form, the device becomes clogged with this solidification, which makes it difficult to continuously and reliably make microcapsules. In order to mediate this, a syringe warming sleeve was purchased to prevent the solution from crystallizing in the syringe, and thermal tape to prevent crystallization in the tubing leading up to the device. However, sodium acetate crystals still formed in the tubing, and we determined that a supersaturated solution could form nucleation sites on the tubing itself. The next step in this process is to find tubing made of a different material that resists the sodium acetate crystallization.

Sodium acetate solution was dispersed in PDMS matrix. SEM images (Figure 20) indicate crystallization inside the droplets after cross-linking the PDMS matrix, although this may be an artifact of the vacuum in the SEM evaporating the water. Encapsulated sodium acetate solutions in polymer capsules is shown in Figure 22. The sodium acetate encapsulated polymer capsules were smooth under optical microscopy and wrinkled in SEM images (Figure 21). The wrinkling may be ascribed to the disappearance of water from the polymer capsules under high vacuum conditions.
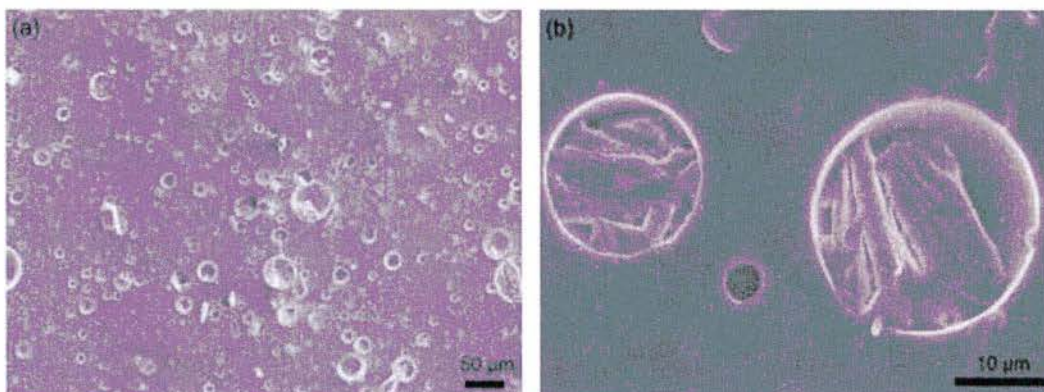

Figure 20. SEM images of the sodium acetate in PDMS matrix after cross-linking.
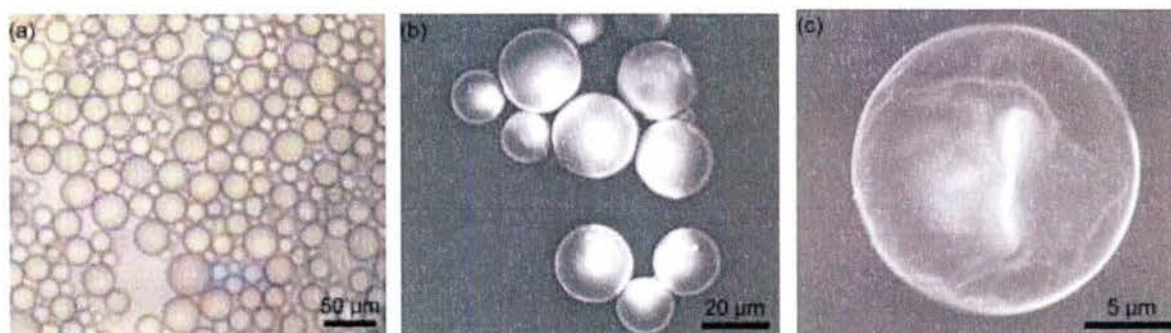
Figure 21. (a) Optical image and (b), (c) SEM images of the capsules encapsulated with sodium acetate solution.

The sodium acetate solution-infilled microcapsules were prepared by forming double emulsions using a microfluidic device. Typically, sodium acetate aqueous solution was used as the inner phase, while UV-cured acrylate was as the middle phase, and poly(vinyl alcohol) in DI water was as the outer phase. The flow rates of the three phases were 2500, 500, and 17000 µl/h, respectively. UV lamps were placed along the collection tube to crosslink the acrylate shells. At last, the prepared microcapsules were collected via a gravity filtering.

Figure 22 shows the three-dimensional image of a sodium acetate solution-infilled microcapsule. It shows a ~280 µm-diameter spherical morphology. From both of the top-view and side-view (right part), the surface of the microcapsule is quite smooth without any crack and defect. More details about core-shell structure and large scale capsules were characterized by scanning electronic microscope (SEM) and optical microscope, respectively, as shown in Figure 23. In the SEM image (Figure 23b), a shell thickness is found to be ca. 2 µm.
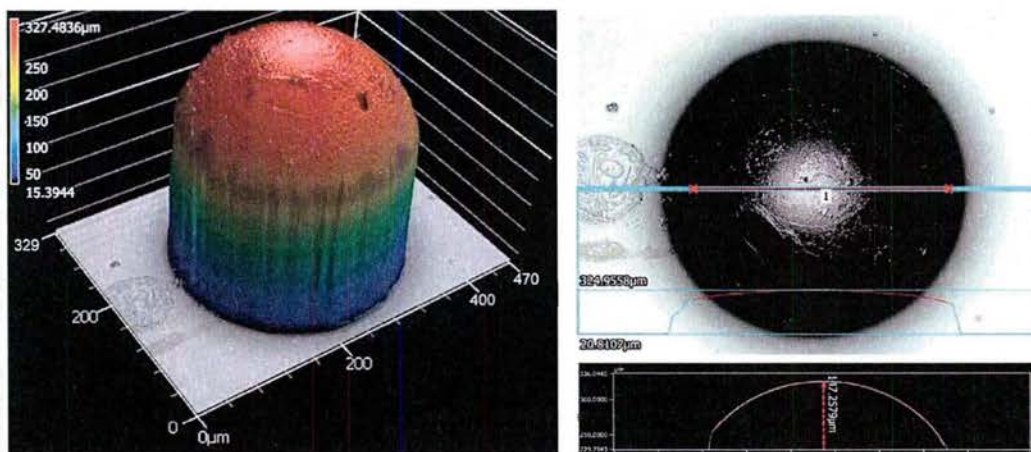

Figure 22. Three-dimensional microscopy image of the sodium acetate solution-infilled microcapsule.
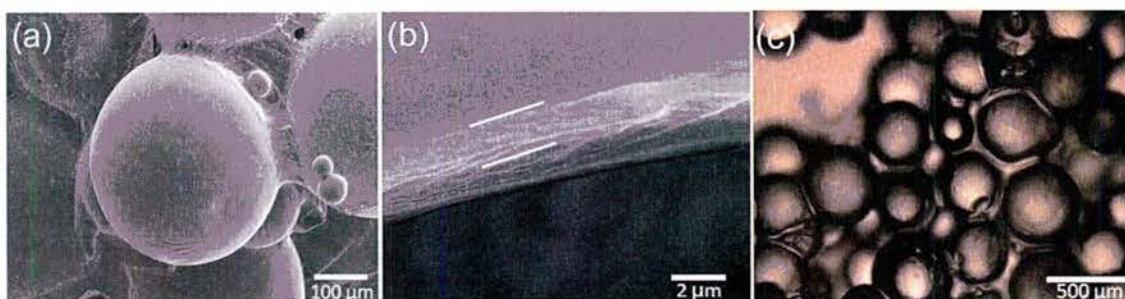
Figure 23. (a), (b) SEM images and (c) optical image of the sodium acetate solution-infilled microcapsules.

In order to show the core content (sodium acetate solution), a series of in-situ optical images were recorded, as shown in Figure 24. Figure 24a confirms the strong strength of the capsule shell which retains the core very well even at a choppy liquid core status driving by heating (~60 °C). In Figure 24b, under a higher heating intensity (~90 °C), seen from a breaking capsule (most of capsules survived), some liquid drops can be clearly observed releasing from capsules.
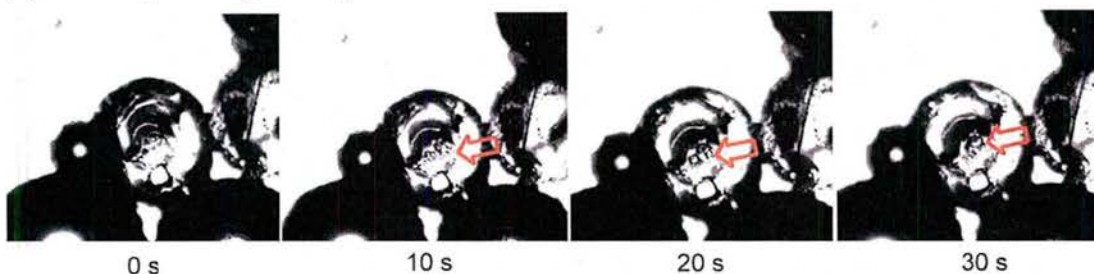
Figure 24. Optical images during *in-situ* observations on sodium acetate solution-infilled microcapsules under different heating intensities: (a) regular intensity, and (b) high intensity.

A series of dynamic mechanical analysis (DMA) were also conducted to investigate the mechanical properties of the matrix. Both at room temperature and -80 °C the Young's modulus were measured, with the consideration that at those temperatures the capsule cores should be liquid and solid, respectively, seen from the DSC results. Current results on the basis of different capsule

contents (from 0% to 16%) in the matrixes have not shown obvious change trends of the mechanical properties, which we will perform more measurements with systematical samples and some specific temperature points.

the encapsulation of sodium acetate solution also received significantly positive progress. In our investigations, the concentration was reduced to much lower than it was previously, 0.67 g mL^{-1} sodium acetate trihydrate in water, in order to avoid premature crystallization before being encapsulated. The solution saturation temperature is well below room temperature, so in order to crystallize, the temperature needs to be decreased to below that. The shell material was also changed to a UV-cured acrylate polymer, as we figured the water permeability would be lower than that of the previous shell material (polystyrene).

An optical microscopy image of the capsules can be seen in Figure 25. The capsule size is about 200 to 300 μm. What's more importantly is that they appear to be stable out of solution. Also, the size distribution is narrow. The SEM images of these capsules are shown in Figure 26. In Figure 26a, the morphology of the capsules seems to be quite smooth, with very few wrinkles or cracks on the shell. The shell thickness can be measured from Figure 26b, where the thickness is estimated to be of ca. 10 μm.
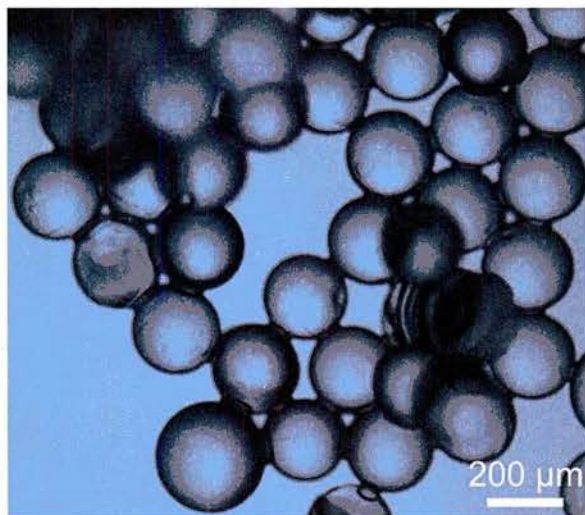

Figure 25. Optical microscopy image of the low concentration (0.67 g mL^{-1}) sodium acetate solutions encapsulated in a UV-cured acrylate polymer capsules.
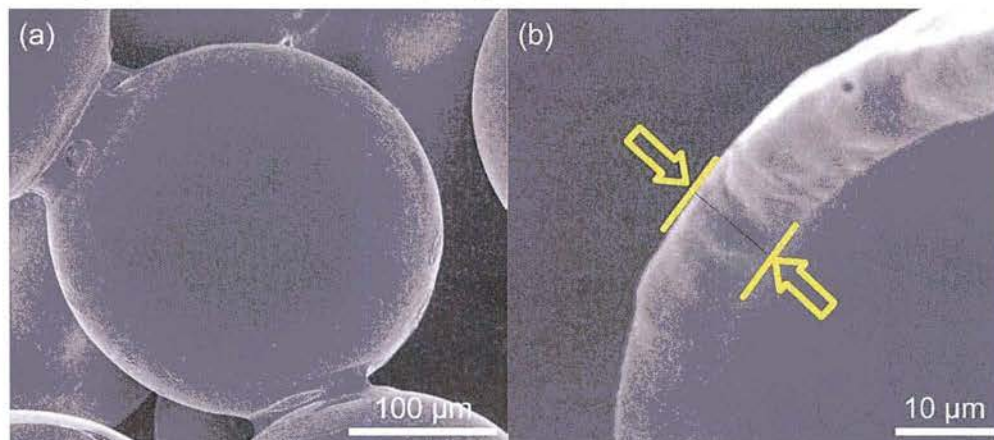
Figure 26. SEM images of the sodium acetate solution-encapsulated microcapsules: (a) surface morphology and (b) shell thickness.

Differential scanning calorimetry (DSC) was also performed on the prepared microcapsules, as shown in Figure 28. The cooling cycles exhibit one large peak at ca. −20 °C, followed by some smaller peaks at around −36 °C, and finally a last peak appears at about −47 °C, respectively. We believe the large peak and the range of smaller peaks are due to heterogeneous nucleation, which nucleates at a higher temperature, while the lowest temperature peak is due to homogeneous nucleation. Going through the DSC cycles, the homogeneous peak shrinks while the large heterogeneous peak rises, possibly indicating that over multiple cycles, the capsules that initially exhibited homogeneous nucleation eventually transit to heterogeneous nucleation.
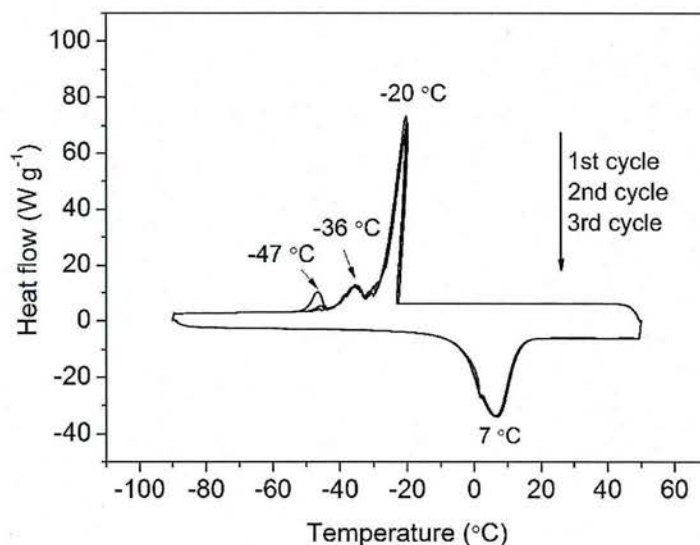
Figure 27. DSC curves (3 cycles) of the sodium acetate solution-encapsulated microcapsules.

The prepared capsules were then dispersed into a PDMS matrix at various volume percentages, as shown in Figure 29. Dynamic mechanical analysis (DMA) was performed on the samples with capsule volume percentages of 0%, 10%, and 20% at room temperature (in which the capsule core contents are liquid), as shown in Figure 30. The Young's modulus drops by about a factor of 2 from 1.25 MPa to 0.59 MPa when increasing the capsule volume percent from 0% to 20%. Experiments have not yet been done on samples below the freezing point of these capsules, but we hypothesize that the modulus will increase substantially with increasing capsule volume percent due to the fact that the mechanical properties of the solid are much stronger than that of the liquid.

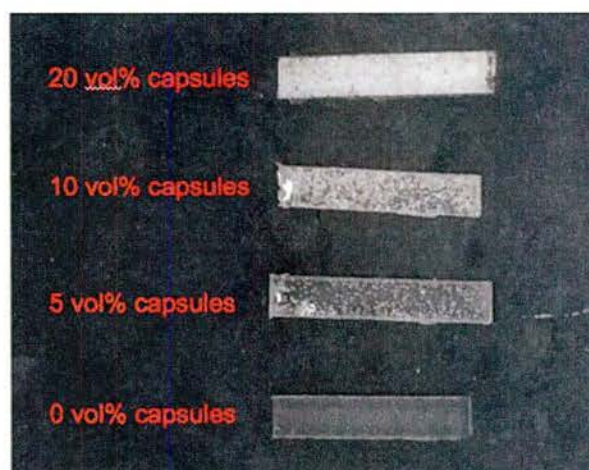**Figure 28.** Picture of the PDMS matrix containing various volume percents of microcapsules
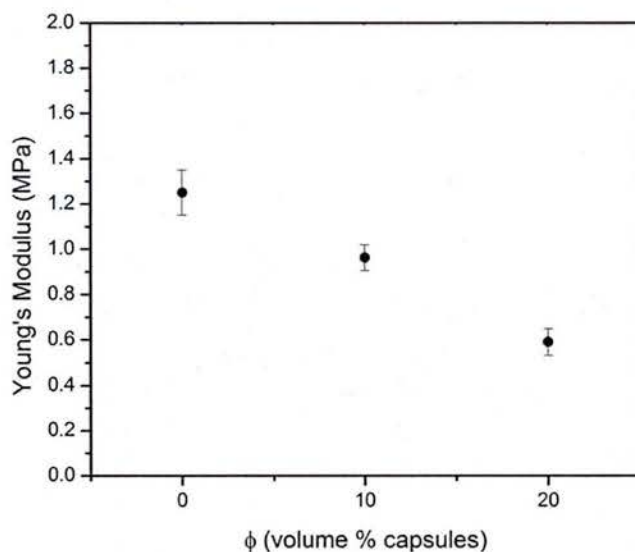
Figure 29. DMA results of the Young's modulus of the PDMS matrix containing 0%, 10%, and 20% microcapsules at room temperature.

About the sodium acetate solution-infilled acrylate microcapsules, we also focused on finding a direct and strong evidence to support our design on the temperature-dependent phase change mechanism. Excitingly, on the basis of a series of explorations, we got some ideal evidences from the cold stage X-ray diffraction (XRD) patterns. In details, as shown in Figure 30, we designed a cycling temperature program in which samples were cooled from room temperature to -90 ℃, then they were heated back to room temperature. During this process, XRD measurements were conducted at the temperatures of -30 ℃ during both cooling and heating. On the basis of our previous differential scanning calorimetry (DSC) results which show that the microcapsule cores

should be liquid at XRD (1) and solid at XRD (2), respectively, we were expecting the phase change-inducted XRD pattern differences at the same temperature under cooling or heating process, which are shown in Figure 31.
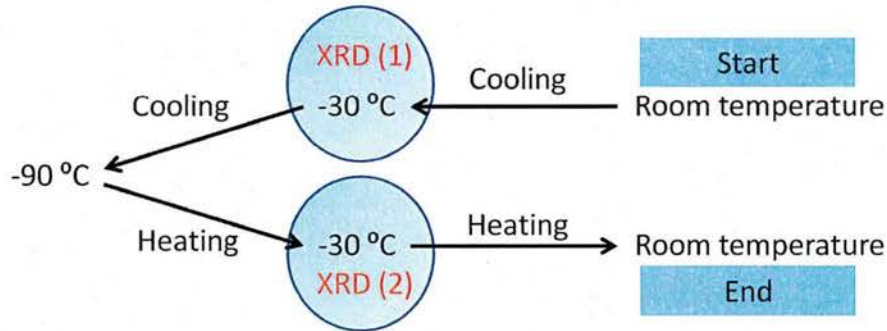
Figure 30. Schematic illustration for the XRD measurements at the temperature of -30 °C under cooling or heating process.
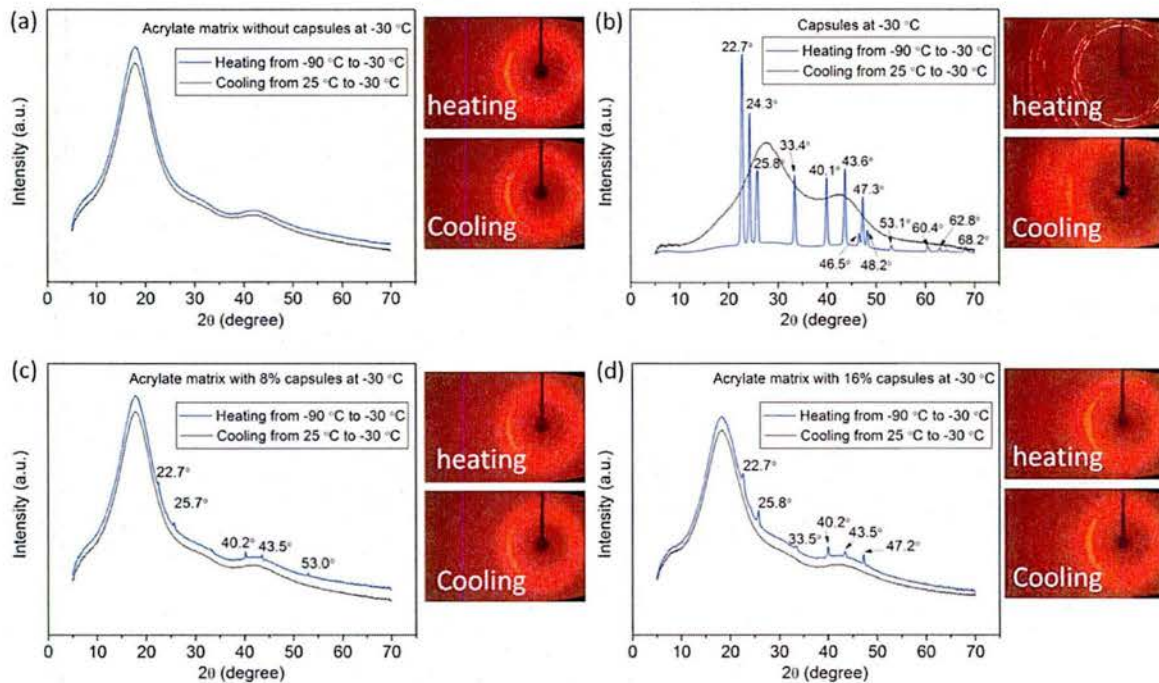
Figure 31. Cold stage XRD patterns obtained at -30 °C on different samples: (a) acrylate matrix without sodium acetate solution-infilled capsules, (b) sodium acetate solution-infilled acrylate capsules, (c) acrylate matrix embedded with 8% sodium acetate solution-infilled capsules, and (d) acrylate matrix with 16% sodium acetate solution-infilled capsules. The insets are the actual diffraction images for each sample.

In Figure 31a, there is no obvious peak difference between heating and cooling processes of the pure acrylate matrix (no sodium acetate solution-infilled capsules), indicating no phase change. However, interestingly, Figure 31 b-d show obviously additional peaks at -30 °C during heating compared to cooling, indicating a crystallization below -30 °C during cooling, and a solid state remained at -30 °C during heating, which are in very good agreement with our previous DSC and dynamic mechanical analysis (DMA) results. In Figure 31 b which was from the sodium acetate solution-infilled capsules, much more intensive peaks can be found. The light spots in the actual diffraction image also well confirm the crystallized core at -30 °C during heating; while the uniforms rings indicate a liquid state of the capsule core during cooling. Even though the microcapsules were embedded into the acrylate matrix, clearly additional XRD peaks which match well with the ones in Figure 31b can still be found, showing the phase change occurs within the matrix. In addition, as shown in Figure 31c and d, depending on the increase of capsule percentage within the matrix from 8% to 16% (volume percentage), the newly appear XRD peaks become more intensive; and more light spots are present in the actual diffraction images during heating, indicating an enhanced phase change behavior with more capsules embedded.

ONR Final Report 2016

Student, Postdoc (PI): Nina Sekerak, Dr. Kristin Hutchins (Moore)

Purpose: We report the controlled syntheses of cross-linked carboxypolystyrene (carboxy-PS) particles ranging in size from 50 nm to 500 μm in diameter. The particles were successfully functionalized to afford, amide, peroxide, and ester bonds. Particles functionalized with benzoyl peroxide were tested as coinitiators and found to be active in the presence of surface and particle-bound dimethylaniline.[1]

We have also successfully functionalized the particles with an ATRP initiator and performed ATRP polymerizations off of the initiator particles. We sought to develop initiator seed particles for frontal polymerizations. These particles were primarily used to study the dynamics of frontal polymerization in the presence of seeds. The effect of seed size on frontal polymerization will also be studied.

Work Completed: Carboxy-PS particles of spanning a wide range of sizes have been synthesized. To obtain the carboxy functionality, 4-vinylbenzoic acid was protected as a *tert*-butyl ester and copolymerized with styrene and a cross-linking agent in an emulsion or suspension polymerization. Emulsion polymerization with sodium dodecyl sulfate as surfactant afforded particles 50 nm in diameter. Surfactant-free emulsion polymerization yielded particles 600 nm in diameter. To obtain particles either 50-200 μm or 100-500 μm in diameter, suspension polymerization was used. Following the polymerization step, the ester was deprotected with trifluoracetic acid in dichloromethane (DCM) to yield carboxy-PS particles. Table 2 summarizes the polymerization conditions for each method, and Figure 32 shows SEM images of the particles before and after deprotection of the acid group.

Table 2. Experimental conditions for synthesis of particles. Sodium dodecyl sulfate (SDS) was used as an ionic surfactant. Mowiol 40-88 (PVA) was used as a steric stabilizer. Potassium persulfate (KPS) and benzoyl peroxide (BPO) were used as initiators.

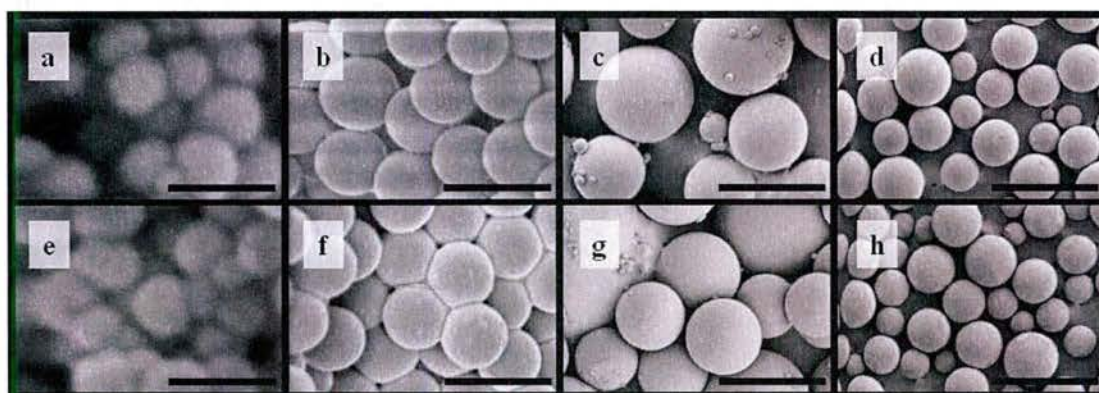| Particle diameter	50 nm	600 nm	50 μm	400 μm
Milli-Q water (g)	250	144	110	110
Surfactant, cosolvent, or stabilizer (g)	0.35 SDS	18.0 MeOH	1.1 PVA	0.25 PVA
Initiator (g)	0.78 KPS	0.23 KPS	0.50 BPO	0.50 BPO
Styrene (g)	19.0	16.1	16.1	16.1
*t*BuVB, initial (g)	-	-	2.0	2.0
DVB (g)	0.96	-	0.18	0.18
*t*BuVB, after 1 h (g)	2.3	2.0	-	-
DVB, after 1 h (g)	0.21	0.18	-	-
Stir rate (rpm)	180	180	400	240

Figure 32 . (a-d) Protected carboxy-PS particles. (e-i) Carboxy-PS particles. Scale bars represent 100 nm in (a) and (e), 1 μm in (b) and (f), 100 μm in (c) and (g), and 1 mm in (d) and (h).

The particles were functionalized to give peroxide, ester, and amide bonds and characterized by scanning electron microscopy (SEM), optical microscopy, diffuse reflectance infrared spectroscopy (DRIFTS), gel-phase ^{13}C NMR spectroscopy, confocal microscopy, and iodometric titration. The cross-linker identity and density in the microparticles has also been studied. Three different cross-linkers were used: divinylbenzene (DVB), ethylene glycol dimethyacrylate (EGDMA), and poly(ethylene glycol) dimethacrylate (PEGDMA). Cross-linker densities of approximately 0.5 mol %, 1 mol %, and 4 mol % were used. In a good solvent, particles with the lowest cross-linking density had volume swelling ratios that were two to three time larger than the particles with the highest cross-linking density. Particles cross-linked with EGDMA were observed to have the largest volume swelling ratios.

Peroxides, which are effective initiators, have been attached to particles of all sizes. The carboxy-PS particles were swollen in a DCM solution of DIC and *m*CPBA overnight followed by washing

with THF and EtOH (Scheme 4). Particles were characterized by gel-phase ^{13}C NMR and IR spectroscopy and by iodometric titration. The titration indicated that the particles had $0.64 \pm 0.02\%$ active oxygen content, which suggests 78% functionalization of the acid functionality. The acid peak was not visible in the IR or NMR spectra, thus, it can be assumed (within limits of detection) that the particles were completely functionalized.
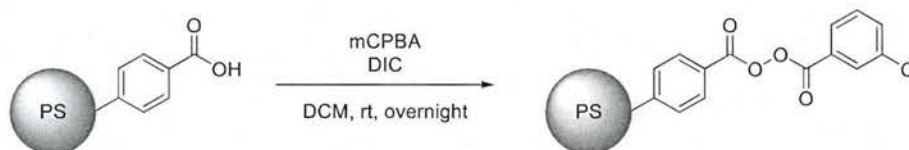
Scheme 4. Synthetic approach to dibenzoyl peroxide (BPO)-functionalized particles.

We sought to determine if the peroxide particles could successfully initiate radical polymerizations in the presence of *N,N'*-dimethylaniline (DMA). The carboxy-PS particles can also be functionalized to incorporate the DMA group (Scheme 5). The carboxy-PS particles were swollen in a solution of dichloromethane, 4-dimethylaminopyridine, and 4-(dimethyamino)benzyl alcohol. Subsequent addition of *N,N'*-diisopropylcarbodiimide afforded DMA-functionalized carboxy-PS particles, which were isolated by centrifugation, washed with THF/EtOH, and dried *in vacuo*. The incorporation of the DMA group was confirmed by gel-phase ^{13}C NMR and DRIFTS.
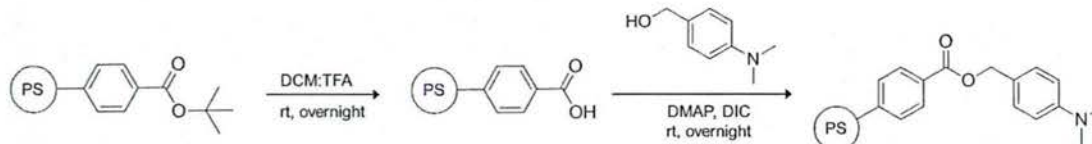
Scheme 5. Synthetic approach to DMA-functionalized particles.

To determine if the BPO- and DMA-functionalized particles could act as radical co-initiators, polymerization of a model monomer, methyl acrylate (MA) was studied. The BPO and DMA particles were placed in a beaker inside a nitrogen-filled glovebag. A stopper was placed on top of the dry beads before addition of MA, and the beads were allowed to swell and react for 1 hr. The beads were removed from the glovebag, washed with THF/EtOH, and dried in vacuo. An ATR-FTIR spectrum of the combined beads indicated signals corresponding to poly(methyl acrylate) (PMA) and SEM images demonstrated a significant increase in polymer bead size for many of the beads (Figure 33). A control experiment was conducted by physically separating the BPO particles from the DMA particles utilizing a cotton barrier. ATR-FTIR spectra of the individual beads did not indicate signals corresponding to PMA and SEM images demonstrated no increase in size for the polymer beads.

DMA beads   BPO beads   combined beads

Figure 33. SEM images of individual beads before polymerization test and combined beads after polymerization test.

To explore the ability of BPO-functionalized particles to initiate polymerization between different surfaces, we also examined reactivity between a particle and a functionalized surface. To yield a DMA-functionalized surface for contact-initiated polymerization, silicon wafers were functionalized according to a literature procedure[2] with the incorporation of N,N-dimethyl-4-((prop-2-yn-1-yloxy)methyl)aniline as the alkyne. The BPO beads were placed on the surface of a DMA-functionalized silicon wafer, which was immersed in a solution of MA at room temperature under ambient atmosphere. A glass stopper was placed on top of the particles on the surface for a period of five minutes. The stopper was removed and the wafer was gently rinsed with milli-Q water, wiped with a Kimwipe, rinsed with ethanol to remove unreacted MA monomer, and wiped with an ethanol-soaked Kimwipe. Optical images of the wafer indicated solid product immobilized on the surface and confocal Raman microscopy exhibited bands from poly(methyl acrylate) (PMA) (Figure 34a). Two control experiments were conducted. One experiment with BPO beads and an azide-functionalized silicon wafer, and a second experiment with carboxy-PS beads and a DMA-functionalized silicon wafer. Optical imaging showed no evidence of solid product on the surface (Figure 34b) and confocal Raman microscopy exhibited no strong signals indicative of PMA formation.
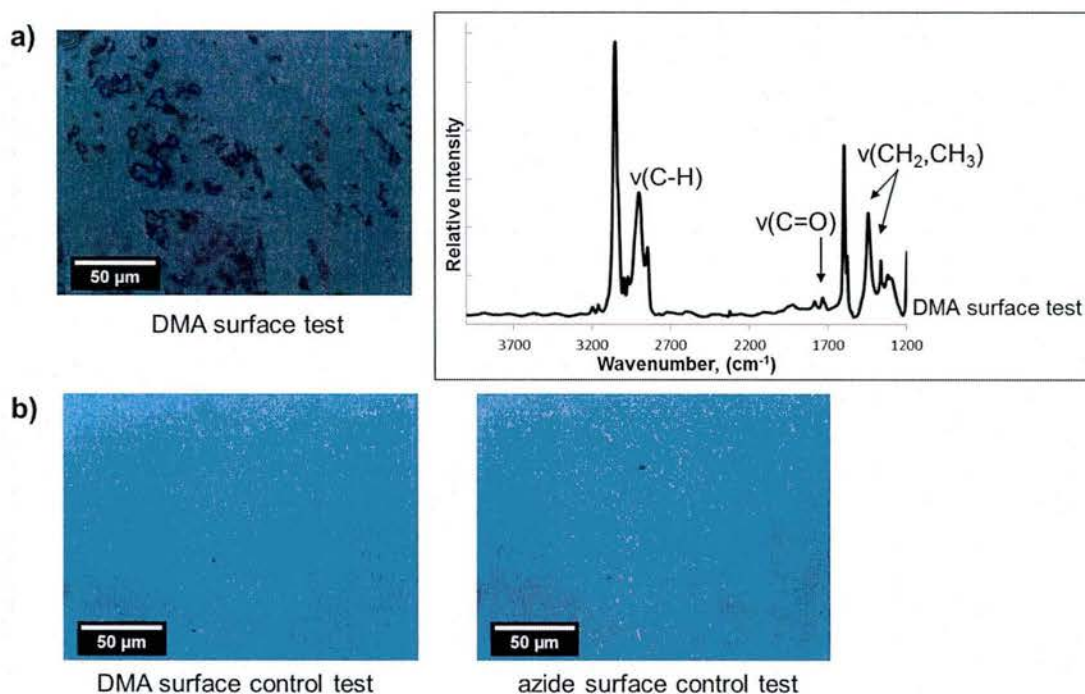
Figure 34. Contact tests: (a) optical images of BPO-DMA contact test and confocal Raman spectrum of surface and (b) optical images of control contact tests.

Particles that are 50-nm and 600-nm in diameter have also been functionalized with an ATRP initiator (Scheme 6). Methyl methacrylate has been successfully polymerized from the particles. The polymer brush has been characterized by DRIFTS and SEM.
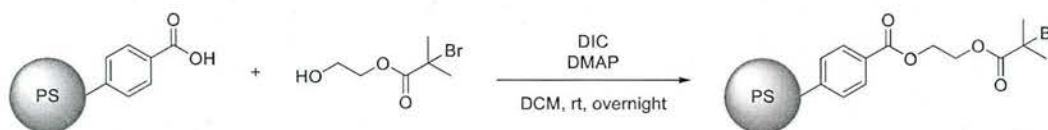
Scheme 6. Synthetic approach to initiator-functionalized particles.

To develop initiator seed particles for frontal polymerizations, we considered utilizing particle-bound peroxide, which was shown to be an active radical initiator. However, the homolytic scission of benzoyl peroxide yielded gaseous byproducts which are problematic to frontal
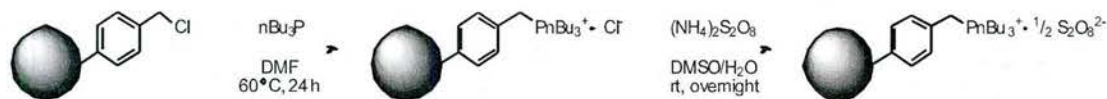
polymerizations in microchannels. Thus, we sought to synthesize another particle-bound initiator that could be implemented in frontal polymerizations. The initiator we chose was analogous to the initiator currently used in our microchannel experiments. The proposed synthesis of the particle-bound initiator is illustrated in Scheme 7.

Scheme 7. Synthesis of particle-bound trialkylbenzylphosphonium persulfate. Particles are crosslinked polychloromethylstyrene before functionalization.

For this synthesis, polychloromethylstyrene particles were needed. Thus, particles approximately 55 nm, 600 nm, and 1.3 μm were synthesized by optimizing literature procedures.[3] This range of particle sizes will allow us to do a series of systematic tests to see whether seed particle diameter affects the reaction. The particles were then functionalized as shown above and characterized by ATR-FTIR spectroscopy. SEM images of the smallest set of particles are shown in Figure 35. Preliminary tests demonstrate that these particles will initiate the free radical polymerization of methyl acrylate and trimethylolpropane triacrylate upon heating. Some of the particles do not withstand functionalization conditions. The crosslinking density can be increased to improve morphological robustness and dispersion techniques can also be optimized. The particles will be tested in frontal polymerizations.
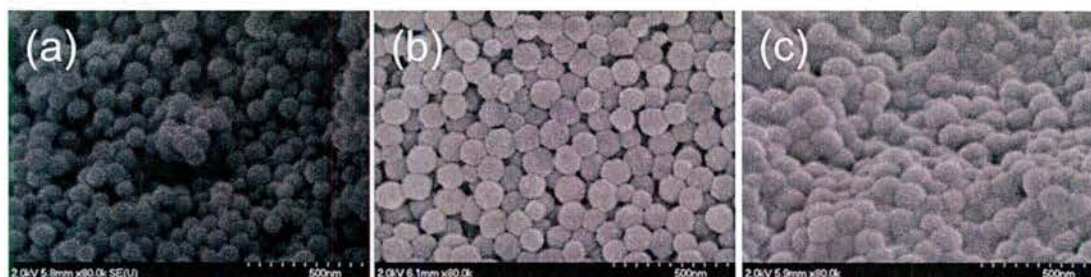

Figure 35. (a) Poly(chloromethylstyrene) nanoparticles, (b) particle-bound trialkylbenzylphosphonium chloride, and (c) particle-bound trialkylbenzylphosphonium persulfate.

References:

1) Horner, L.; Schwenk, E. *Angew. Chem.* **1949**, *61*, 411.
2) Lummerstorfer, T.; Hoffmann, H. *J. Phys. Chem. B* **2004**, *108*, 3963.
3) (a) Chonde, Y.; Liu, L.-J.; Krieger, I. M. *J. Appl. Polym. Sci.* **1980**, *25*, 2407. (b) Margel, S.; Nov, E.; Fisher, I. *J. Polym. Sci. Part A* **1991**, *29*, 347.

Student (PI): Jun Li (Moore)

Purpose: It has been reported by the Moore group and other research groups that mechano-chemically active motifs can be activated by elongation flow and mechanical stretching when incorporated within polymer chains, yet proved to be non-active when present in small molecules or at the end of a polymer chain. Whether mechanophores can be activated when attached at hetero-

interfaces and how the interface property will alter the activation behavior is worth exploring to broaden the usable mechanochemistry systems. The equivalence of elongation flow and mechanical stress in terms of energy transduction to the mechanophore makes solution sonication methods, which could generate elongation flow through collapse of cavity, an ideal and feasible way to test the activity of mechanophore. However, when mechanophore is embedded at the interface of hetero-substances, how the collapse of cavity will drive the polymer and therefore the mechanophore is another interesting question to be answered.

Work Completed: The interface at spherical solids was chosen due to easiness of modification and characterization. Silica nanoparticles were utilized as a model for spherical solids because it provides a clear difference in thermal decomposition temperature of the solid matrix and attached polymer. An anthracene-maleimide based mechanophore was synthesized and designed to anchor on the surface of silica nanoparticles to test the activation behavior.
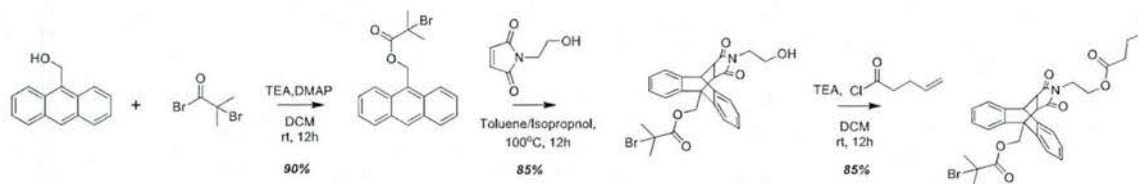
Scheme 8. Synthesis of double-bond functionalized anthracene-maleimide based mechanophore initiator.

A double-bond functionalized anthracene-maleimide based mechanophore initiator was synthesized in three steps, all of which had a yield over 85% (Scheme 8). The double bond was introduced to suit the reaction with silane and therefore the immobilization on silica nanoparticles. The structure was confirmed with ^{1}H NMR, ^{13}C NMR, mass spectrometry (ESI), and elemental analysis of Br.

With the collaboration with Professor Bin Zhao's group at University of Tennessee, the conversion of double-bond functionalized mechanophore initiator to silane functionalized mechanophore initiator was completed. The resultant mechanophore initiator silane was immobilized on the surface of 20 nm (d) silica nanoparticles. With two different kinds of silane reagent, the immobilization resulted in grafting density of 0.3 chain/nm^2 and 0.1 chain/nm^2 (Scheme 9). ATRP polymerization of *tert*-butyl acrylate was then conducted to receive mechanophore-anchored hairy nanoparticles.
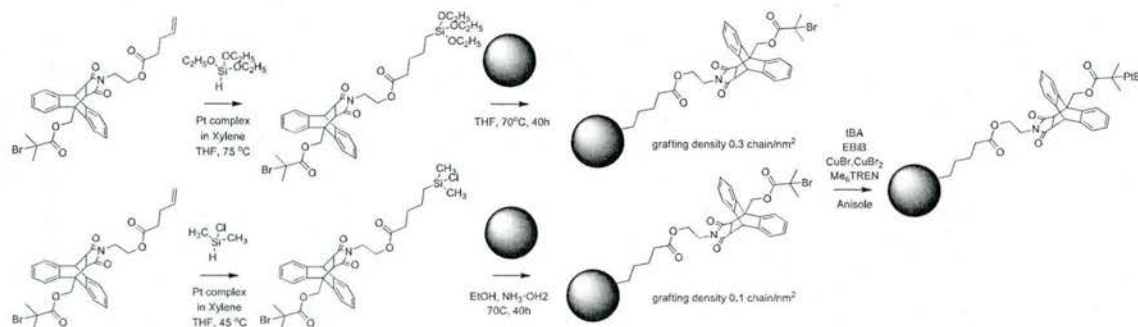
Scheme 9. Synthetic routes of immobilization and polymerization of hairy nanoparticles.

Sonication protocols will be utilized to examine the activation behavior of the mechanophore. Scheme 10 illustrates the proposed mechanical response of the hairy particles upon sonication; a retro [4+2] cycloaddition is expected at the maleimide-anthracene (MA) linkage. To test this hypothesis, preliminary experiments were performed.
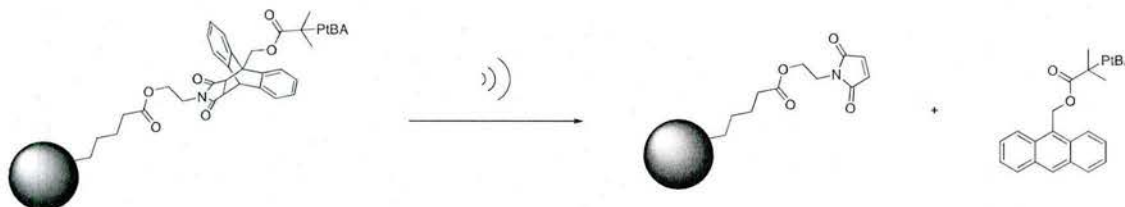
Scheme 10. Proposed mechanical cleavage of a polymer brush attached to a silica nanoparticle via a maleimide-anthracene (M-A) linkage.

Mechanical force was applied by solvodynamic shear generated with an ultrasound acoustic field. As shown in Figure 36a, when subjected to ultra-sonication for a sufficient amount of time, i.e. 6 hrs (Figure 36a, red line) in comparison with 10 mins (Figure 36a, black line as a control), the mechanophore-anchored hairy SiO_2NPs exhibited a distinct cleavage of attached polymer chains, which was observed by gel permeation chromatography (GPC). To further investigate whether the polymer cleavage resulted from selective activation of the mechanophore, UV absorption spectra of the detached polymer, sonicated for 10 min (Figure 36b) and 6 hrs (Figure 36c), were measured in the GPC (retention time 27.5 min) using a photodiode array detector. As evident in Figure 36b and 36c, the polymer cleaved from the surface of SiO_2Nps exhibited identical absorption bands as the reference polymer that was synthesized from an anthracene ATRP initiator (Figure 36d). The characteristic absorption peaks of the anthracene unit (255, 332, 348, 364 and 385 nm) were observed for the cleaved polymer, suggesting a selective retro [4+2] cycloaddition at the interface of the SiO_2Nps and PtBA polymer brush.
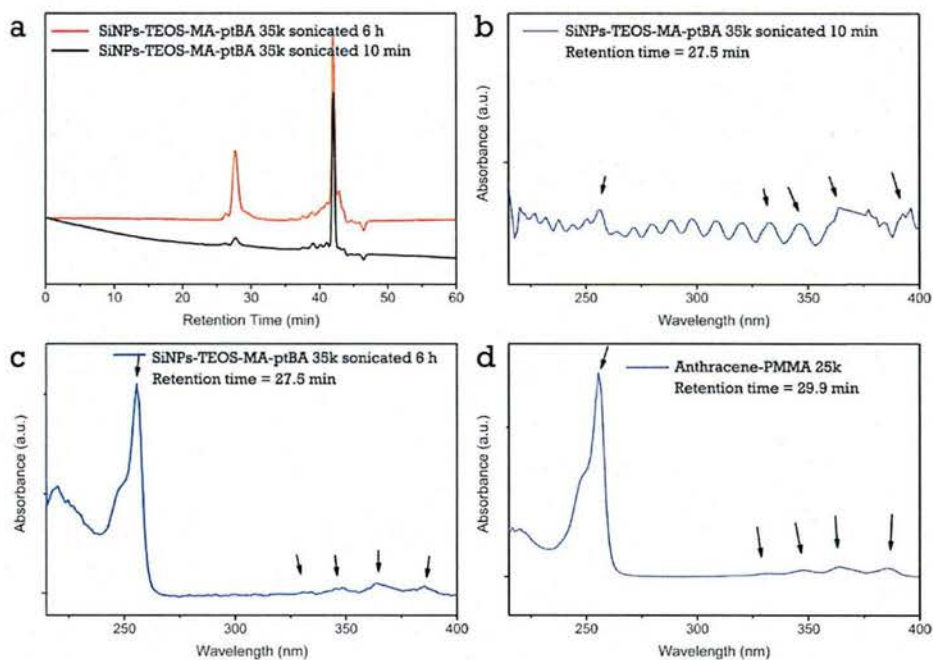
Figure 36. (a) GPC (UV@254nm) trace of M-A mechanophore anchored PtBA-SiO₂ nanoparticles following ultra-sonication for 10 min (black line) and 6 hrs (red line). (b) UV absorption spectrum of GPC eluent following 10 min of ultrasonication at a retention time of 27.5 min. (c) UV absorption spectrum of GPC eluent following 6 hrs of ultrasonication at a retention time of 27.5 min. (d) UV absorption spectrum of reference anthracene end-capped polymer.

A series of kinetic studies were conducted to examine the reactivity of the mechanophore when present at interfaces. Grafted SiO₂Nps (SiO2-TEOS-MA-PMA-40k) were subjected to ultrasonication experiments (0.5 s on; 1.0 s off; 25% power level), and proportions of solution were injected into GPC at 10 min, 30 min, 60 min, 90 min, 120 min, 150 min, 180 min, 210min, 240 min, 270 min, 300 min, 330 min, 360min, respectively (Figure 37a).
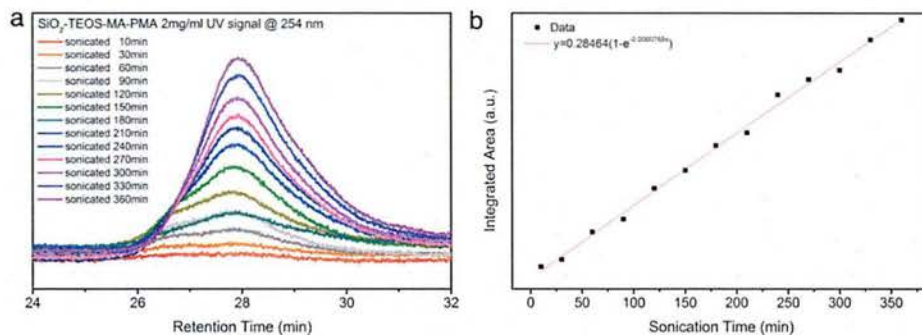

Figure 37. Kinetic study of SiO₂-TEOS-MA-PMA-40k.

Integration of the polymer absorption at 254 nm was plotted against sonication time, and the resultant trend was fitted to the first-order reaction function y = A*(1-exp (-B*x)). The kinetic constant was determined as $7.7 * 10^{-5}$ min⁻¹. All kinetics studies were conducted three times to

ensure accuracy. Different molecular weight polymer grafted nanoparticles with targeted MW = 40k, 30k, 20k, 10k, 5k were synthesized.

Following sonication, the grafted nanoparticles underwent a change in particle interactions as by TEM (Figure 38). Before activation, SiO$_2$ particles were stabilized by the grafted poly(methyl acrylate) (Figure 38a, 38b). After 6 h of sonication, the cleavage of the polymer brush yielded aggregations of nanoparticles (Figure 38c, 38d).
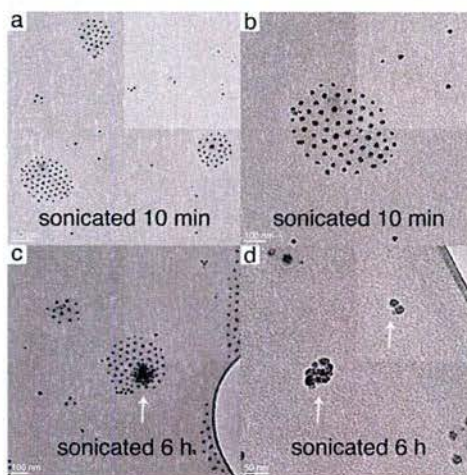

Figure 38. TEM of grafted particles after 10 min and 6 h sonication.

A control polymer was synthesized from bifunctional M-A mechanophore initiator using single electron transfer living radical polymerization (SET-LRP) (Scheme 11). The activity of the linear polymers will be compared to that of the brush grafted to the particles. A series of kinetic studies were conducted to examine the reactivity of the mechanophore placed at the center of a PMA polymer. As shown in Figure 39, MA-centered PMA was subjected to ultra-sonication experiments (0.5 s on; 1.0 s off; 25% power level). Aliquots of the solution were removed from the reaction mixture and analyzed by a GPC with a UV-vis detector at regular time intervals (Figure 39a). The UV absorption pattern of a sonicated, 100-kD sample exhibits a similar signature trace to the sonicated particles shown in Scheme 10. The absorption at 254 nm is credited to the anthracene chromophore released upon mechanophore activation. Integration of the absorption peak at 254 nm in the GPC trace was plotted against sonication time. The resultant trend was linear. All kinetics studies were conducted three times to ensure accuracy.
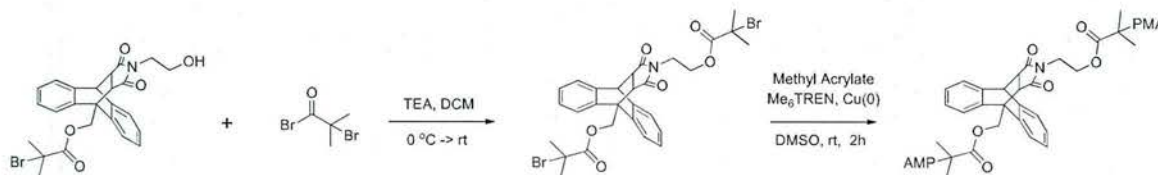
Scheme 11. Synthetic routes of M-A mechanophore centered poly(methyl acrylate).
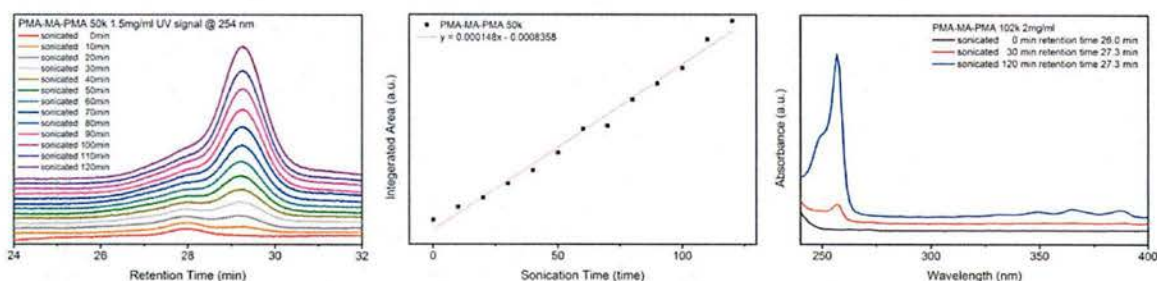
Figure 39. (a) GPC trace of 50-kD polymer, (b) kinetic study of PMA-MA-PMA-50k and (c) UV signal of PMA-MA-PMA-100k.

The kinetic coefficient of mechanical activation of MA in a linear polymer was calculated. For a first-order reaction, e.g. R = P + T,

$$[P] = \left(1 - e^{-kt}\right) * [R]_0 .$$

For a low-rate, low-conversion reaction (usually < 10% conversion),

$$[R] \approx [R]_0$$

and

$$[P] = k[R]_0 t .$$

The UV trace observed is

$$\int AdV = \varepsilon d \int CdV$$

where A is absorption, ε is the extinction coefficient of 113000 L*mol^{-1}*cm^{-1}, d is the path length (d = 1 cm), C is the concentration, and V is the volume. Concentration of the product is then

$$[P] = \frac{n}{V^*} = \frac{\int AdV}{\varepsilon dV^*}$$

where V* is the volume of the aliquot injected into GPC (40 μL). Thus, the equation that relates the kinectic coefficient to the intergration of the peak is

$$\int AdV = k\varepsilon dV * [R]_0 t.$$

This is the equation for the trendline in Figure 37b. Therefore, the slope of the trendline is equal to $k\varepsilon dV * [R]_0$, from which the kinetic coefficient k can be calculated. The calculated coefficient k varied from 3×10^{-4} min^{-1} to 1×10^{-3} min^{-1}.

As shown above, the kinetic coefficient of the mechanochemical reaction was calculated from the equation $\int AdV = k\varepsilon dV * [R]_0 t$. By varying the molecular weight of the polymer attached to the interface, the nature of mechanochemical reactivity of the detachment is elucidated. Along with relevant controls, we demonstrated that the rate of the retro-cycloaddition reaction increased with chain length, thereby proving our theory of mechanochemical selectivity. As shown in Figure 40, a linear increase in the kinetic coefficient was observed for increasing molecular weight (Figure 40, black squares). The trend for polymer-grafted particles was compared to that of MA-centered linear PMA (PMA-MA-PMA) (Figure 40, red circles). For both the linear polymer and the polymer-grafted particles, a linear relationship between the kinetic coefficient and molecular weight of the polymer was observed. Additionally, the threshold molecular weight for the particle-bound polymer is similar to PMA-MA-PMA. These results reveal that when present at interfaces, the activation of polymer-bound mechanophores still follows the same principles as their homopolymer counterparts. We conclude that the data for the homopolymer system such as

threshold molecular weight and reaction kinetics will be useful in guiding the design of mechanophore-functionalized composite interfaces.
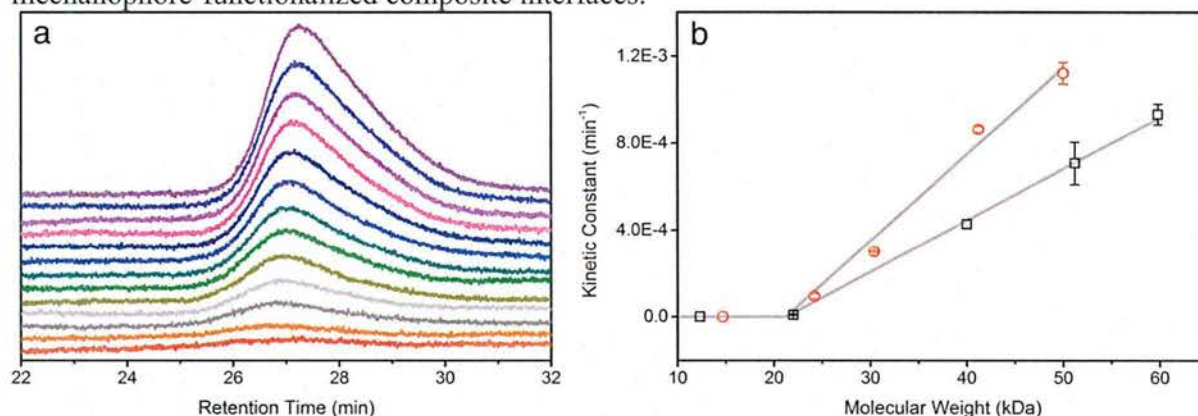

Figure 40. (a) GPC trace of SiO$_2$NPs-MA-PMA-50k, 2 mg/mL in THF, at 3, 10, 20, 30, 40, 50, 60, 70, 80, 90, 100, 110, 120 min ultrasonication. (b) Molecular weight dependence of first order kinetic coefficient for reactions conducted at 5 °C in the SiO$_2$NPs-MA-PMA series (black square, slope = 2.38E-5, r^2 = 0.96) and the PMA-MA-PMA series (red circle, slope = 4.51E-5, r^2 = 0.99).

In the previous investigations on heterogeneous mechanophores, there was one intriguing experiment that caught our attention. The common grafting density of our samples is 0.3 chain/nm^2, while the sonication test on a 0.1 chain/nm^2 experiments displayed a much higher activation rate. We recognized this phenomenon to be of high importance, because the grafting density is a key factor in the design of self-healing composite materials. There were two hypotheses that might help explain how the grafting density could affect the activation rate: crowdedness at the interface may affect a) initial orientation of mechanophore or b) efficiency of mechanical force transduction to the mechanophore.
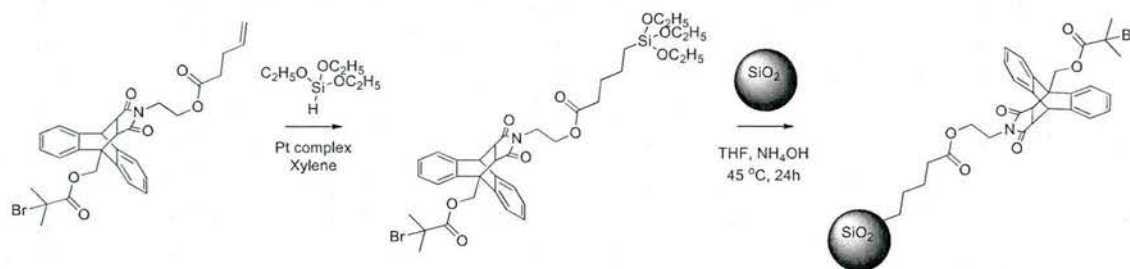
Scheme 12. Immobilization steps to anchor the mechanophore-initiator on silica nanoparticles.

As shown in Scheme 12, in the immobilization step, we varied the amount of initiator-modified triethoxysilane (Int-TEOS) added to control the grafting density of the initiator on the surface (note: control initiators were first used to establish the immobilization technique). Using the aforementioned surface-initiated single-electron-transfer living radical polymerization along with TGA experiments, the grafting densities were determined. For now, we are able to precisely control the grafting density at 0.1, 0.2, 0.3 chain/nm^2, and we have synthesized MA-mechanophore-anchored SiO$_2$NPs in these three grafting densities accordingly.
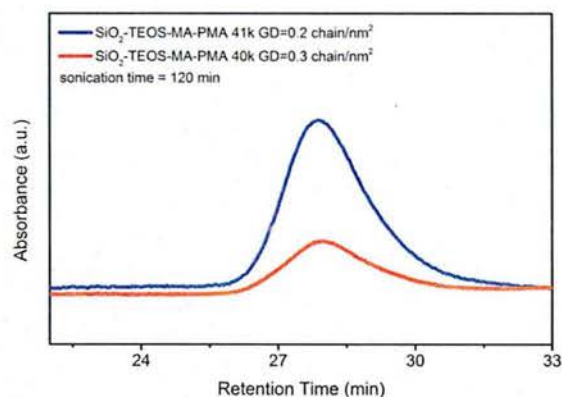
Figure 41. GPC trace of mechanochemically-cleaved polymer in 0.2 chain/nm^2 samples (blue) and 0.3 chain/nm^2 samples (red).

As shown in Figure 41, after obtaining silica nanoparticle particle grafted with poly(methyl acrylate) (0.2 chain/nm^2), subjection to ultrasonication resulted in cleavage of polymer chains due to mechanochemical response of the anthracene-maleimide anchoring point. This result accords with what was previously reported in our manuscript.[1] More importantly, direct comparison of the GPC trace of 0.2 chain/nm^2 samples (Figure 41, blue) and 0.3 chain/nm^2 (Figure 41, red) reveals the fact that a lower surface crowdedness is more favorable for mechanochemical activation events. The integration of the peaks reflects a ca. 3 times activeness difference of a same mechanophore anchored at surfaces of different surface crowdedness. The conclusion is very important for future design of mechanoresponsive composite materials because grafting density of polymer brushes at interfaces is a key parameter.
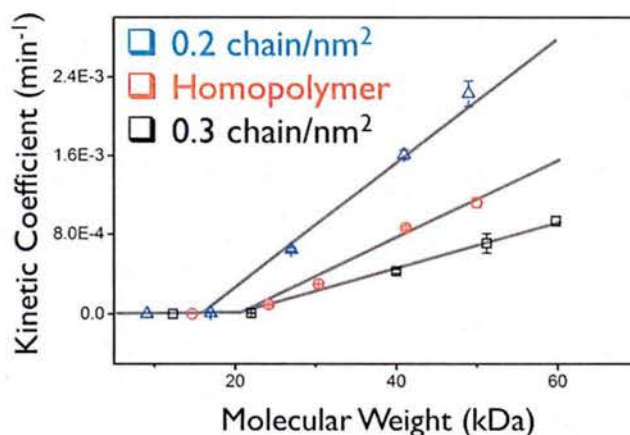

Figure 42. Molecular weight dependence of kinetic coefficient of mechanochemical reaction in homopolymer (red), 0.2 chain/nm^2 sample (blue) and 0.3 chain/nm^2 (black).

To further identify the effect of lower surface crowdedness on activation efficiency and understand the underlying cause, our efforts were focused on variation of grafting density of initiator

nanoparticles and the kinetic studies. As shown in Figure 42, by varying MW of the grafted chain and comparing with homopolymer systems, a reduction of threshold MW and higher activation rate in low grafting density samples were observed. This result reconfirms the previous conclusion that lower grafting density allows higher mechanochemical activation rate. With this observation, our initial hypothesis that higher mass on one side of mechanophore should enable higher reactivity was now partially validated. More importantly, the conclusion that lower surface crowdedness is more favorable for mechanochemical activation events is extremely valuable for future design of mechanoresponsive composite materials because grafting density of polymer brushes at interfaces is a key parameter. The remaining question now becomes why lower surface crowdedness enables higher activation rate. We proposed that it may be related to a) polymer morphology and b) air bubble nucleation and growth, both of which are directly related to surface crowdedness.

To further identify the validity of the hypothesis that nucleation process of gas bubbles is dependent of the uncovered surface area of nanoparticles, which varies in samples of different grafting density, our efforts were focused on using DPPH assays to quantify the nucleation events and how addition of silica particulates affects the nucleation speed.
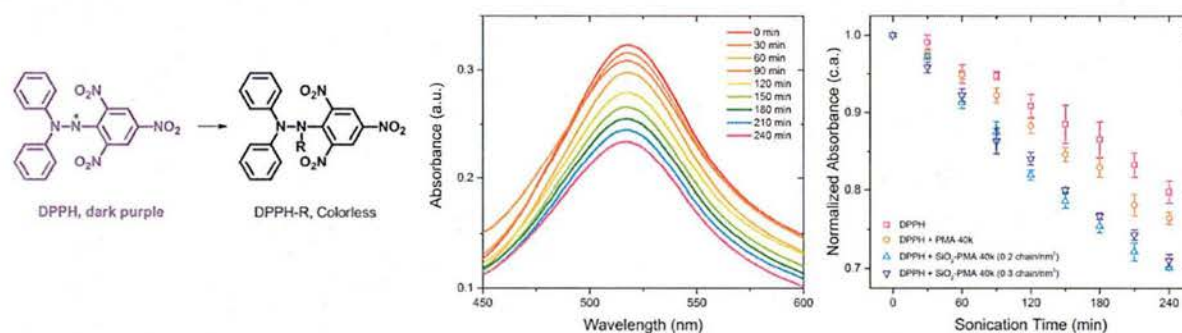

Figure 43. Scheme of bleach mechanism of 2,2-diphenyl-1-picrylhydrazyl (DPPH) (left), time dependent UV spectra of sonicated DPPH solutions (middle), and comparison of bleaching speed of DPPH at the presence of poly methacrylate (PMA), lower grafting density PMA grafted silica nanoparticles and higher grafting density PMA grafted silica nanoparticles (right).

As shown in Figure 43 (left), 2,2-diphenyl-1-picrylhydrazyl (DPPH) is stable radicle that possess dark purple when dissolved in solution (THF). Upon sonication, nucleation and collapse of gas bubbles lead to extreme temperature and pressure at the center of collapse, converting DPPH to DPPH-R (R = solvent molecule, DPPH or degradation product in solution). As a result, the dark purple color is bleached. DPPH thus was used here to monitor the rate of gas bubble nucleation and collapse in various sonication studies. As an example, the UV spectrum of DPPH solution presented in Figure 43 (middle) demonstrated the gradual bleaching of DPPH and its absorbance at 520 nm was plotted against sonication time to visualize the bleaching rate. Shown in Figure 43 (right), bleaching rate of DPPH (pure THF solution, pink squares) slightly decreased at the addition of 1.8 mg/ml poly(methacrylate) (PMA) (40 kDa) (orange circles), while addition of PMA-grafted silica nanoparticles (purple and blue triangles, amount normalized to weight of SiO_2) led to

noticeable decrease of DPPH bleaching. However, no observable difference was found in two series of samples with different grafting density of PMA chains.

Thus, it is concluded that 1) presence of nano-particulate accelerates nucleation and collapse of gas bubbles; however 2) nucleation and collapse process of samples with different grafting densities is found almost identical and thus is not the direct cause of the difference in mechanochemical activation rate.

References:

1) Li, J.; Shiraki, T.; Hu, B.; Wright, R. A. E.; Zhao, B.; Moore, J. S. *J. Am. Chem. Soc.* **2014**, *136*, 15925-15928.

2) Li, J.; Hu, B.; Yang, K.; Zhao, B.; Moore, J. S. *ACS Macro Lett.* **2016**, *5* (7), 819–822.

Rapid Stiffening of a Microfluidic Endoskeleton via Frontal Polymerization

Student (PI): Ian Robertson (Moore)

Purpose: We report composite materials that have the ability to rapidly stiffen themselves via a propagating frontal polymerization (FP) that produces an endoskeletal structure within a flexible material. (Figure 44) The FP process increases Young's modulus up to 18x and allows for freestanding structures to be rapidly fabricated.
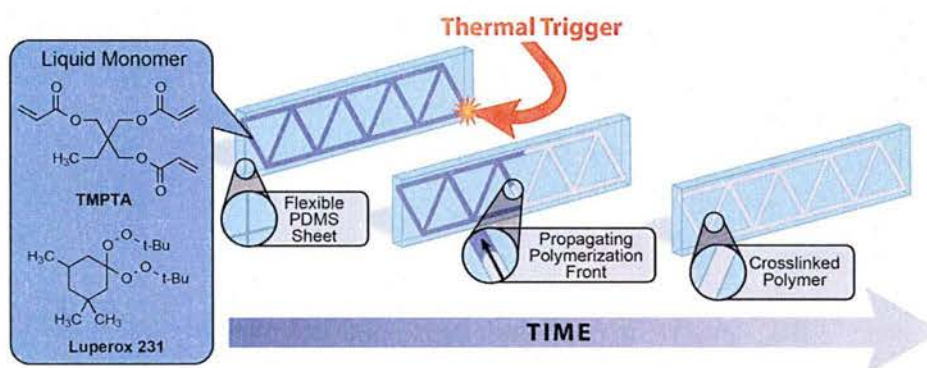

Figure 44. Schematic illustration of frontal polymerization within a microchannel endoskeletal network. Before frontal polymerization is initiated, the material is a highly flexible PDMS sheet encapsulating microchannels filled with reactive liquid monomer and initiator, shown in purple. A concentrated source of thermal energy initiates a polymerization front that quickly spreads throughout the microvascular network, effectively reinforcing the entire sample with rigid, crosslinked polymer, shown in gray.

Work Completed: As microchannel diameter impacts heat transfer and front quenching based on the surface-area-to-volume ratio of the channel, a limiting channel size through which a frontal polymerization propagates for a given reaction and matrix composition is expected. To test the limitations of our chemistry, a series of straight, cylindrical channels ranging from 723 µm to 1120

μm in diameter were fabricated. Initiation was tested on 50 mm lengths of each channel diameter. The results were recorded on video and the following parameters were calculated: average propagation distance, percentage complete propagation, and average front speed (Table 3). Based on this data, the limiting size for the chemistry reported here lies between 762 μm and 838 μm, where the propagation reached the critical diameter allowing >50% of the samples to completely propagate. The 762 μm channels show propagation rarely occurring, and limited to less than 10 mm when present. The majority of 838 μm channels allowed complete propagation. Below 762, there were no instances of propagation; and above 838, propagation through the whole sample was almost always observed. The speed of the front decreased as it approached the cutoff limit of 762 μm. This decrease indicates that the level of heat loss affects propagation. Above 1100 μm, front speed was observed to be approximately 20 cm/min, similar to the front speed observed in cm-scale reaction vessels. Consequently, a 5-cm sample can be stiffened in as little as 15 seconds.

Channel Diameter (um)	Average Propagation Distance (mm)	Percentage Complete Propagation	Average Front Speed (cm min^{-1})
723	1	0	-
762	6	12.5	15.4
838	16	63	17.8
1100	50	100	20.4

Table 3. Samples 50 mm in length with single microchannels of several diameters were assessed in terms of average distance of propagation, percentage of samples that allowed propagation of the whole sample with a single initation, and average front speed.
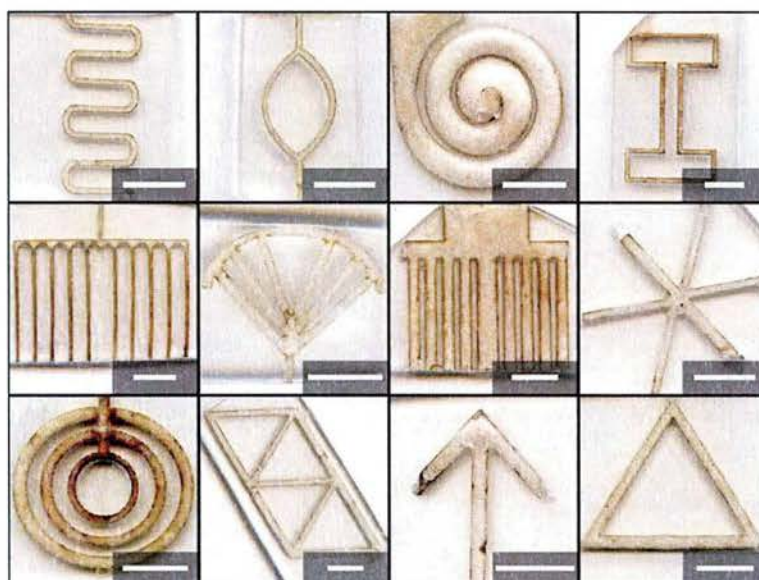

Figure 45. A variety of frontally polymerized geometries are demonstrated.

Further investigation into versatility of front propagation within different microchannel geometries has been performed as shown in Figure 45. The results show that geometry posed almost no hindrance to polymerization. Fronts could successfully propagate through converging geometries as well as angles, curves, and most branches. The one problem that was observed with regard to geometry was in terminal perpendicular branching, in which propagation only proceeded through one branch of the channel, leaving the other branch unreacted. The unreacted channels were still reactive when initiated from the opposite end, suggesting the monomer solution was not the cause of this effect. We suspect small bubbles would accumulate at the front and be shunted to one side as the propagating wave reached the branch. These bubbles made the front preferentially prefer one path over the other. To circumvent this, the perpendicular junction points were expanded slightly to allow room for the bubbles to move without disrupting the propagation process.

Having better understood the versatility of frontal polymerization within vascular networks, we wanted to assess the mechanical reinforcement such a reaction would impart on a flexible composite consisting of Sylgard 184 PDMS reinforced by polyTMPTA rods. Changes in Young's modulus for straight channel composite samples were examined. Tensile tests were performed in the longitudinal direction of the microfluidic channels. Samples with unidirectional channels and varying volume percents from 0–15 % were created by increasing the number of 1.12 mm channels in the sample from 0–5 while keeping the overall dimensions of the PDMS constant. The mechanical stiffening imparted by the formation of polyTMPTA within the channels was investigated through dynamic mechanical analysis and shown to increase the Young's modulus of tensile samples by a factor of 18 in samples with 15 vol. % reinforcement, which corresponded well with the rule of mixtures prediction (Figure 46).
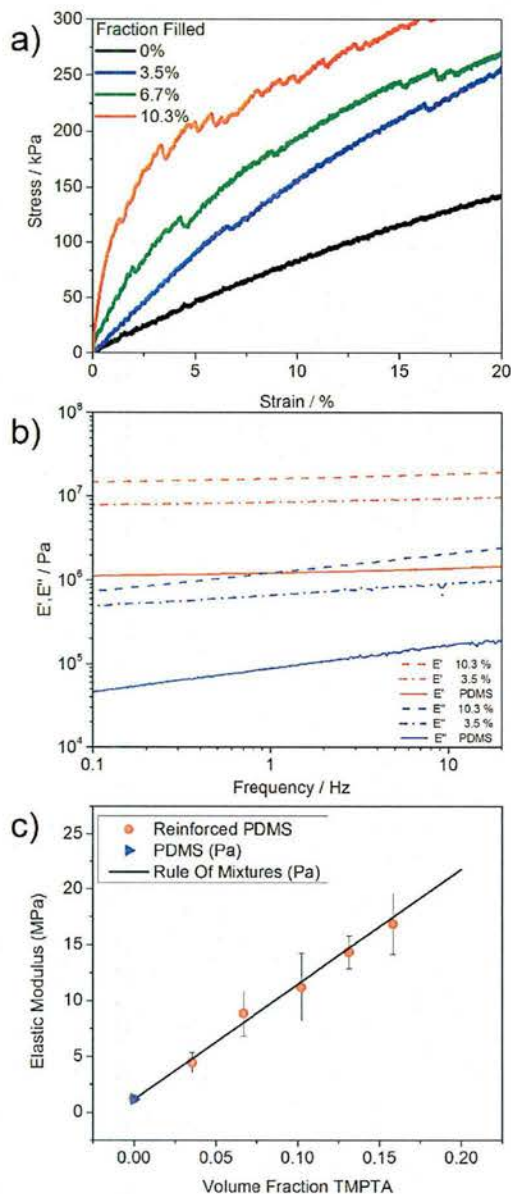
Figure 46. The effect of frontally polymerized channels on the mechanical properties of PDMS composites. (a) Representative stress-strain curves for Young's modulus measurements up to 20% strain. The fracture of polyTMPTA reinforcement at large strains results in nonlinearity in stress response. (b) Frequency response of the storage and loss moduli of the composite samples with increasing polyTMPTA volume percent. (c) Young's moduli for samples with 1-5 channels. The modulus increases with increasing vol % and is in agreement with the rule of mixtures. Error bars represent one standard deviation (n=3).
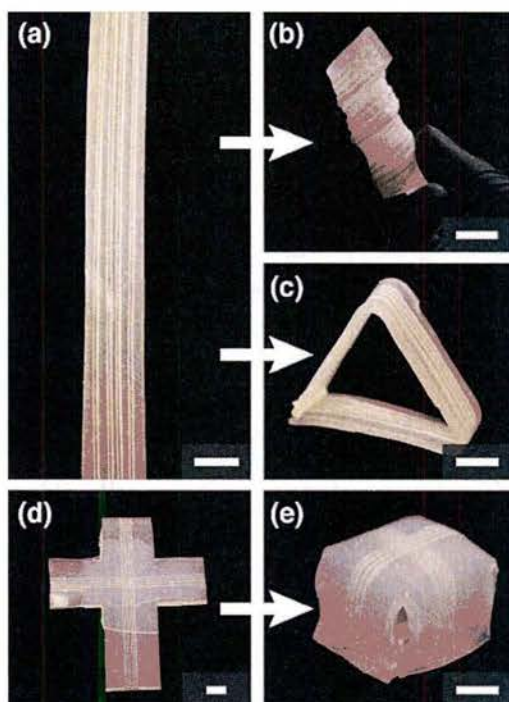
Figure 47. Embedded microchannels used to flash-cure PDMS into a variety of shapes. (a) Several straight segments of Ecoflex PDMS with four linear 1120-µm channels were fabricated. (b) One segment was wrapped around a ¾ inch rod into a helical shape. Frontal polymerization was spot-initiated at one end, and propagation through the whole channel was complete in approximately one minute. The helix retains its shape after being removed from the rod. (c) A similar 4-channel segment of Ecoflex PDMS was flash-cured into a free-standing triangle. (d) A layer-by-layer fabrication introduced 2 sets of channels into a t-shaped piece of PDMS. (e) This pattern allowed for the formation of a cube, which retained its shape after polymerization was performed within the channels. All scale bars are 1 cm.

To demonstrate the utility of this method of stiffening, several samples with linear channels of 1120 µm in diameter were filled with reactive monomer and initiator, deformed into different shapes, and subsequently spot-initiated. The frontal polymerization flash-cured the system in less than one minute. After the maintaining force was removed, the samples retained their shapes, reflective of enhanced rigidity (Figure 47). These results were published in *ACS Applied Materials and Interfaces* in October 2014.

References:

(1) Robertson, I. D.; Hernandez, H. L.; White, S. R.; Moore, J. S. *ACS Appl. Mater. Interfaces* **2014**, *6* (21), 18469–18474.